Experiments versus theory for the initiation and propagation of radial hydraulic fractures in low permeability materials

B. Lecampion[1], J. Desroches[2], R.G. Jeffrey[3],A.P. Bunger[4,5]

[1]Geo-Energy Lab - Gaznat chair on Geo-Energy, Ecole Polytechnique Fédérale de Lausanne,

EPFL-ENAC-IIC-GEL, Switzerland

[2]Schlumberger, Paris, France

[3]SCT Operations Pty Ltd, Vic., Australia

[4]Department of Civil and Environmental Engineering, University of Pittsburgh, PA, USA

[5]Department of Chemical and Petroleum Engineering, University of Pittsburgh, PA, USA

Key Points:

- Quantitative agreement between experiments and theoretical predictions of fracture initiation and evolution (pressure, length, width) in low permeability materials
- Clarification of the mechanisms involved in radial hydraulic fracture initiation and early-growth via dimensional analysis
- Introduction of a dimensionless number to quantify the difference between initiation and breakdown pressures as function of injection and material parameters.

Corresponding author: B. Lecampion, `Brice.Lecampion@epfl.ch`

Abstract

We compare numerical predictions of the initiation and propagation of radial fluid-driven fractures with laboratory experiments performed in different low permeability materials (PMMA, cement). In particular, we choose experiments where the time evolution of several quantities (fracture width, radius, wellbore pressure) were accurately measured and for which the material and injection parameters were known precisely. Via a dimensional analysis, we discuss in detail the different physical phenomena governing the initiation and early stage of growth of radial hydraulic fractures from a notched wellbore. The scaling analysis notably clarifies the occurence of different regimes of propagation depending on the injection rate, system compliance, material parameters, wellbore and initial notch sizes. In particular, the comparisons presented here provide a clear evidence of the difference between the wellbore pressure at which a fracture initiates and the maximum pressure recorded during a test (also known as the breakdown pressure). The scaling analysis identifies the dimensionless numbers governing the strong fluid-solid effects at the early stage of growth, which are responsible for the continuous increase of the wellbore pressure after the initiation of the fracture. Our analysis provides a simple way to quantify these early time effects for any given laboratory or field configuration. The good agreement between theoretical predictions and experiments also validates the current state of the art hydraulic fracture mechanics models, at least for the simple fracture geometry investigated here.

1 Introduction

The propagation of hydraulic fractures has received continuous attention since the pioneering work of *Khristianovic and Zheltov* [1955]; *Hubbert and Willis* [1957]; *Geertsma and De Klerk* [1969]. The combination of elasticity, linear elastic fracture mechanics and lubrication flow inside the fracture yields a stiff non-linear system of equations for the time evolution of fracture extent, width and fluid pressure distribution in the fracture. It is only over the past three decades that a better understanding of the multi-scale nature of hydraulic fracture propagation has emerged [*Spence and Sharp*, 1985; *Lister*, 1990; *Desroches et al.*, 1994; *Lenoach*, 1995; *Garagash and Detournay*, 2000; *Garagash et al.*, 2011], highlighting the difficulty of obtaining accurate numerical solutions. Analytical or semi-analytical solutions have also been obtained for some particular fracture geometries (radial, plane-strain) in some limiting cases where one mechanism dominates the

dissipation of energy during the propagation (resistance to viscous fluid flow, or creation of new fracture surface for example) - see *Detournay* [2016] for a review.

In parallel, many experimental investigations have also been carried out since the late 1950s [see e.g. *Hubbert and Willis*, 1957], although proper measurements of fracture extent and width distribution versus time are absent from early contributions, which typically only report borehole pressure versus time and the fracture geometry at the end of the test. The use of transparent materials have enabled measurements of both fracture extent and spatial width distribution during fracture growth. Such experiments have allowed complete comparisons with theoretical predictions, see *Bunger and Detournay* [2008]; *Bunger et al.* [2013] for experiments in glass and PMMA, or the recent experiments of *Lai et al.* [2015] in hydrogel. In the case of experiments performed in rocks or other opaque materials, the evolution of the fracture extent can be obtained from ultrasonic measurements. Using acoustic plane-wave reflection, it is also possible to measure fracture width [*Medlin and Masse*, 1984; *Groenenboom and Fokkema*, 1998], see also *Kovalyshen et al.* [2014] for a comparison between ultrasonic and optical methods for the measurement of fracture width. Passive acoustic emission monitoring is also often used for monitoring hydraulic fracture growth at the laboratory scale (see *Lockner and Byerlee* [1977]; *Stanchits et al.* [2015] among many others), providing an indirect measurement of the evolution of the fracture extent. Little in-depth comparisons between theoretical predictions and experiments have been reported so-far for non-transparent materials. Moreover, most of the comparisons between experiments and theory have focused solely on the propagation stage and neglected the transient effects associated with hydraulic fracture initiation from the wellbore, which may be dominant at the laboratory scale in some cases [*Bunger et al.*, 2005; *Lhomme et al.*, 2005].

The goal of this paper is to compare hydraulic fracturing laboratory experiments performed in different tight materials (PMMA, cement) with theoretical predictions from a numerical solution of the governing equations of hydraulic fracture mechanics, including fracture initiation from a finite size wellbore. We focus solely on transverse radial hydraulic fractures initiating from a radial notch at the wellbore wall and propagating in an isotropic material, as depicted in Figure 1. Such a geometry is the simplest one amenable to precise experimental investigations while exhibiting all the coupled non-linear effects associated with hydraulic fracture initiation and propagation. With respect to field applications, it corresponds to a vertical fracture transverse to a horizontal wellbore: a con-

figuration which is different from the typical bi-wing vertical fracture from an un-cemented vertical wellbore. It is important to note that we assume fracture initiation to occur from an initial defect, i.e. the onset of propagation (not just opening) of that defect. Nucleation of a fracture from an initially defect free material can be investigated using the concepts of finite fracture mechanics (e.g. *Leguillon* [2002]; *Cornetti et al.* [2006]) or via cohesive zone models (e.g. *Lecampion* [2012a]). However, in practice, due to the drilling or perforation process, defects are always present at the wellbore wall, such that assuming that a hydraulic fracture initiates from a pre-existing defect is realistic. Extension of the present model to fracture initiation in a defect free material is deferred to a subsequent contribution (see *Lecampion* [2012b] for the case of a plane-strain hydraulic fracture nucleating from a wellbore).

In this paper, we highlight different effects associated with fracture initiation, such as the influence of the well pressurization rate (i.e. injection rate and system compliance), fluid viscosity, initial notch size and their influence on the early stage of hydraulic fracture growth. We use dimensional analysis to describe the different time- and length-scales associated with these different phenomena. We notably pay attention to the difference between the initiation pressure (the wellbore pressure at which the fracture initiates) and the breakdown pressure (a misnomer which simply corresponds to the maximum pressure recorded during an injection test). This difference stems from the strong viscous effects at play during wellbore pressurization, fracture initiation and early propagation (i.e. fluid entrance in the newly created fracture). It has been observed on a number of experiments [*Weijers*, 1995; *Zhao et al.*, 1996; *Stanchits et al.*, 2013] and discussed theoretically for plane-strain conditions [*Detournay and Carbonell*, 1997; *Lakirouhani et al.*, 2016]. We will clarify which dimensionless parameters control the difference between the fracture initiation pressure and the maximum pressure.

We first briefly review the governing equations of hydraulic fracture mechanics, highlighting the importance of the wellbore and injection system at initiation and during the early stage of fracture growth. We restrict ourselves to linear elastic fracture mechanics and only slightly permeable materials where fluid leak-off -if any- can be approximated by a one dimensional diffusion process perpendicular to the fracture faces. Using dimensional analysis, we define the transitions between early-time propagation regimes (affected by the injection system and the finite wellbore size) and late-time propagation regimes (where the hydraulic fracture propagates as in an infinite medium under a constant in-
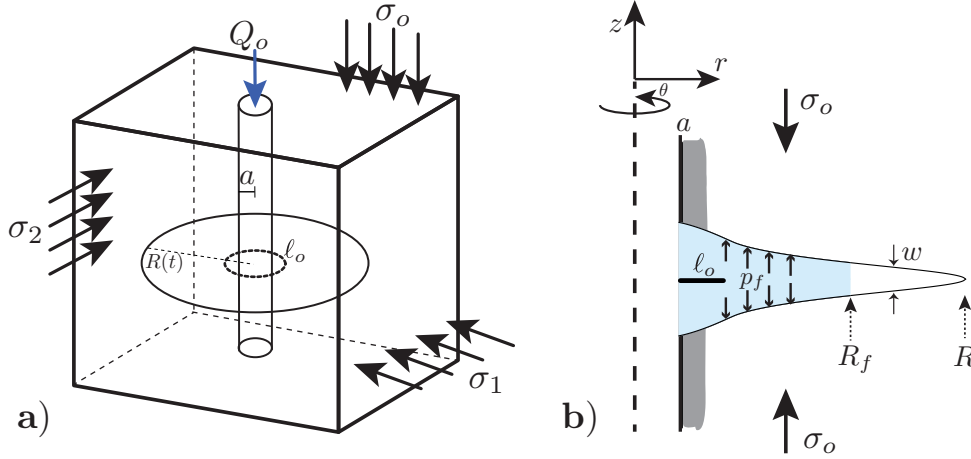
Figure 1. a) Sketch of the experimental configuration of a radial fracture transverse to a wellbore of radius a in a block under compressive stresses ($\sigma_o < \sigma_1 < \sigma_2$). b) corresponding axisymmetric model. The fracture initiates from an axisymmetric notch of depth ℓ_o perpendicular to the minimum far-field stress σ_o.

jection rate). We then perform an in-depth comparison of theoretical predictions with three experiments performed in different materials under two different types of propagation regime (toughness or viscosity dominated).

2 Hydraulic fracture mechanics

We restrict our discussion to a planar radial hydraulic fracture initiating transversely to a wellbore of radius a from an initial axisymmetric notch of extent ℓ_o transverse from the borehole wall, normal to the in-situ minimum stress (see Fig. 1). Modeling of hydraulic fracture initiation and propagation combines the elastic deformation of the material, fluid flow within the created fracture under the hypothesis of lubrication theory, leak-off from the fracture faces and the linear elastic fracture mechanics propagation condition. We briefly recall the governing equations of the problem, allowing for the possible existence of a fluid lag at the fracture tip. We also pay particular attention to the fluid compressibility in the injection line which turns out to have a strong effect during the early stage of growth.

2.1 Governing equations

For a strictly opening mode axisymmetric fracture, the elasticity equations reduce to the following boundary integral equation relating fracture width w and the normal net loading $p = p_f - \sigma_o$ (net pressure) acting on the fracture plane (see e.g. *Hills et al.* [1996]):

$$p_f(r) - \sigma_o = p = E' \int_a^{R(t)} g^{wb}(r, r'; a) \frac{\partial w}{\partial r'} \mathrm{d}r' \tag{1}$$

where $E' = E/(1-\nu^2)$ is the plane strain Young's modulus. The kernel $E' \times g^{wb}(r, r')$ represents the stress component normal to the fracture plane at r induced by a unit axisymmetric dislocation ring of radius r' around a cylindrical cavity of radius a. Its expression is given in *Keer et al.* [1977] in terms of Hankel transform - note that it depends weakly on the material Poisson's ratio, see also *Lecampion and Desroches* [2015] for discussion on the weak effect of the finite wellbore. For such a configuration of a transverse axisymmetric fracture from a cemented wellbore, it is important to note that the stress concentration induced by wellbore pressurization does not play any significant role on the elastic equation (1). This is a notable difference with the more classical case of the initiation of a longitudinal fracture from an un-cemented well [e.g. *Haimson and Fairhust*, 1967; *Lecampion*, 2012b; *Lakirouhani et al.*, 2016]. The most classical occurence being the case of a vertical fracture in a vertical well under a normal stress regime.

Under the assumption of a slightly compressible liquid of compressibility c_f, the width averaged mass conservation in the fracture reduces to the following continuity equation in axi-symmetry:

$$\frac{\partial w}{\partial t} + w c_f \frac{\partial p_f}{\partial t} + \frac{1}{r} \frac{\partial}{\partial r}(rq) + g_l(r, t) = 0. \tag{2}$$

for $r \in [a, R_f]$, where R_f denotes the boundary of the fluid filled region of the fracture. The fluid compressibility term $w c_f \partial p_f / \partial t$ is typically much smaller than the width variation term $\partial w / \partial t$ (see Appendix A: for details) and will be subsequently neglected. The leak-off rate from the fractures faces g_l is modelled here via the early-time solution of the 1D linear diffusion equation perpendicular to the fracture face (Carter's leak-off model as discussed in *Howard and Fast* [1957]). Such an approximation is valid for tight rocks and a sufficiently short injection duration (see e.g. *Kovalyshen and Detournay* [2013] for a complete discussion):

$$g_l(r, t) = \frac{C'}{\sqrt{t - t_o(r)}}$$

163   where $t_o(r)$ is the time at which the fluid front has reached the radius r; $t - t_o$ is thus

164   the exposure time of the fracture faces to the fracturing fluid at a given location r and

165   $C' = 2C_L$, where C_L is Carter's leak-off coefficient (and the factor two stems from the

166   fact that fluid leaks off from the two opposite faces of the created fracture). Note that,

167   for some limiting cases, the exact value of C_L can be derived from rock and fluid param-

168   eters. However, in the more general case, the value of C_L is a lumped parameter whose

169   value is determined experimentally (see *Smith and Montgomery* [2015]).

170   Under the lubrication approximation, the fluid flow inside a fracture is approximated

171   locally as the steady-state fully-developed pressure driven flow between two parallel plates.

172   The width-averaged balance of momentum under these approximations reduces to Poiseuille's

173   law [see e.g. *Batchelor*, 1967] which relates the local fluid flux $q = w V$ to the local pres-

174   sure gradient

$$q = -\frac{w^3}{\mu'} \frac{\partial p_f}{\partial r} \tag{3}$$

175   where $\mu' = 12\mu_f$, μ_f is the fracturing fluid viscosity and V is the fluid velocity.

176   In the case of the presence of a fluid lag, the fluid pressure in the lag zone is uni-

177   form and equal to the fluid cavitation pressure p_{cav}, which is typically negligible com-

178   pared to the in-situ confining stress σ_o [*Garagash and Detournay*, 2000; *Garagash*, 2006],

179   such that:

$$p_f - \sigma_o = p = -\sigma_o \qquad \text{for } r \in [R_f(t), R(t)]. \tag{4}$$

180   The Stefan condition at the boundary between the fluid front and the lag $r = R_f(t)$

181   reads

$$\frac{\mathrm{d}R_f}{\mathrm{d}t} = -\frac{w^2}{\mu'} \frac{\partial p_f}{\partial r} \qquad \text{at } r = R_f \tag{5}$$

182   The boundary condition at the fracture inlet at the wellbore wall is:

$$2\pi a \, q(r = a, t) = Q_{in}(t) \tag{6}$$

183   where Q_{in} is the flow rate entering the fracture at time t, which results from the inter-

184   action of the flow in the fracture with the flow in the injection system (injection line and

185   wellbore) as will be discussed shortly. A local fluid pressure drop term at $r = a$ is some-

186   times used to account for entry pressure losses through geometrical restrictions not ex-

187   plicitly modeled at the fracture/wellbore junction. It is, for example, the case in-situ,

188   when the junction between the cemented well and the fracture is achieved via perfora-

189   tions. In laboratory experiments, when using a radial notch as depicted in Fig.1, such

190   a junction is usually smooth and one can assume that the fluid pressure is continous at

191     $r = a$.

192   The fracture is assumed to propagate under quasi-static equilibrium in opening mode,

193   such that the stress intensity factor K_I equals the material fracture toughness K_{Ic} once

194   the fracture has initiated:

$$K_I = K_{Ic} \tag{7}$$

195   We estimate the stress intensity factor from the linear elastic fracture tip asymptote for

196   width (e.g. *Rice* [1968]):

$$w \sim \sqrt{\frac{32}{\pi}} \frac{K_I}{E'} \sqrt{R - r} \qquad R - r \ll 1 \tag{8}$$

197   Initiation of the hydraulic fracture will thus occur when the stress intensity factor reaches

198   K_{Ic} and the hydraulic fracture will subsquently propagate under quasi-static equilibrium

199     $K_I = K_{Ic}$ at all time. For simplicity of notation, we will use $K' = \sqrt{\frac{32}{\pi}} K_{Ic}$ in the

200   remainder of the paper.

201   *Fluid flow in the injection system*   The integration of the fluid mass balance over

202   the whole injection system (of volume V_{inj}), i.e. between the pump and the fracture in-

203   let gives:

$$Q_{in} = Q_o - U \frac{\partial p_f}{\partial t} \tag{9}$$

204   where U (dimensions $[m^3/Pa]$) is the total injection system compliance. It is mostly gov-

205   erned by fluid compressibility $U \sim c_f V_{inj}$ where V_{inj} is the total volume of the injec-

206   tion system, but deformation of the wellbore and injection lines may also play a role. Prior

207   to fracture initiation, the flow rate entering the fracture Q_{in} is negligible, which for a con-

208   stant injection rate Q_o results in a linear pressurization rate $\partial p_f / \partial t = (Q_o/U)$. The

209   injection system compliance U can thus be directly obtained from the slope of the pres-

210   surization phase (prior to fracture initiation) knowing Q_o. One can alternatively use ei-

211   ther U or Q_o/U to quantify the effect associated with the storage of fluid in the injec-

212   tion system prior to fracture initiation, but we settle for the injection system compliance

213   U. After fracture initiation, due to the fluid viscous resistance, the fluid pressure in the

214   wellbore may continue to rise while the entering flow rate slowly increases. After break-

215   down (i.e. maximum pressure), the amount of fluid stored by compressibility during the

216   pressurization phase will enter the fracture such that the flow rate entering the fracture

217   Q_{in} will temporaly exceed the pump rate Q_o. Once this transient associated with early

218   time growth vanishes, the entering flow rate Q_i tends to the injection rate Q_o.

For sufficiently long wellbores such as those typically used in the oil and gas industry, a significant pressure drop from fluid friction necessarily occurs along the length of the well. This is typically not the case in the laboratory where the injection system is short enough. However, in some cases, either on purpose (e.g. placing a needle valve in the flow line) or because of the presence of a measurement device in the wellbore (e.g. for measuring the width), a local pressure drop actually takes place. This is the case for two of the experiments reported here (PGMY8 and COV12c), for which we have accounted explicitly for such a frictional drop. This is done by modeling the complete fluid flow in the wellbore, accounting for local friction if necessary, in conjunction with hydraulic fracture initiation and propagation (see *Lecampion and Desroches* [2015] for more details), a coupling which is necessary for field configurations (long wellbore, significant pipe friction, presence of perforations, etc.).

2.2 Numerical Solution

Although semi-analytical solutions exist for some limiting cases [*Savitski and Detournay*, 2002], there is no solution available for the complete transition from initiation to the late stage of propagation. In the following, we therefore use a numerical model recently developed [*Lecampion and Desroches*, 2015] solving the set of equations previously described for the initiation and propagation of a radial hydraulic fracture from a wellbore. This numerical simulator is based on a fixed grid and an implicit time-stepping scheme. The elasticity is solved using the displacement discontinuity method, while fluid flow is discretized via finite volume. The resulting non-linear system of equations (for a trial value of the new position of the fracture front) is solved using fixed-point iterations. In that numerical model, the presence of a fluid lag is not taken into account explicitly: the fluid pressure is allowed to be lower than the cavitation pressure. The evolution of the fracture front during one time-step is obtained via the implicit level set algorithm first proposed by *Peirce and Detournay* [2008], see also *Detournay and Peirce* [2014]. Such a scheme is based on the complete tip asymptotic solution for a steadily moving hydraulic fracture [*Garagash and Detournay*, 2000; *Garagash et al.*, 2011]. More details on the numerical scheme - including the effect of wellbore flow and compressibility-can be found in *Lecampion and Desroches* [2015], where the case of multiple radial hydraulic fractures initiating transverse to the wellbore is also treated. This numerical simulator has been validated against a number of available reference solutions [*Savitski and*

Detournay, 2002; *Madyarova*, 2003] and compared to a previous contribution based on a different propagation scheme [*Abbas and Lecampion*, 2013].

2.3 Regimes of propagation

Initiation and propagation of a hydraulic fracture is a highly non-linear moving boundary problem governed by a series of physical mechanisms (elasticity, fracture mechanics, fluid flow, leak-off). The response of the system can vary widely depending on which of these effects dominates (or not) over the others. Scaling and dimensional analysis are of utmost importance to properly understand the different limiting regimes of propagation. Scaling also allows design of laboratory experiments that are relevant with respect to field conditions. The complete dimensional analysis is presented in Appendix A: and a Mathematica notebook is given in the Supplementary Materials for completeness.

2.3.1 Infinite medium - constant entering flow rate

The case of a radial hydraulic fracture propagating in an infinite medium (without wellbore, i.e. $a = 0$) under constant injection rate (limiting case where $U = 0$ and $Q_{in} = Q_o$ as a result of eq.(9)) has been thoroughly studied [*Geertsma and De Klerk*, 1969; *Abé et al.*, 1976; *Cleary and Wong*, 1985; *Savitski and Detournay*, 2002; *Madyarova*, 2003]. In particular, the propagation of such a radial hydraulic fracture has been shown to transition from a viscosity dominated regime of propagation at early time to a toughness regime of propagation at large time. This can be understood intuitively as the energy spent in creating an increment of fracture surface becomes larger as the fracture perimeter ($2\pi R$) increases. Fracture energy (toughness) therefore dominates the propagation of radial hydraulic fractures at large time. On the other hand for small fracture radius/early time, viscous flow dissipation is the main dissipative mechanism and controls the hydraulic fracture propagation. A dimensionless toughness $\mathcal{K} = (t/t_{mk})^{1/9}$ governs the transition from the viscosity to the toughness dominated regime with time and $t_{mk} = \dfrac{E'^{13/2}Q_o^{3/2}\mu'^{3/2}}{K'^9}$ is the transition time-scale between these two regimes. The toughness regime of propagation is reached when $\mathcal{K} \gtrsim 3.5$ [*Savitski and Detournay*, 2002]. In the presence of fluid leak-off, another time-scale enters the problem (see *Madyarova* [2003] for details), a situation that is not dominant in the experiments reported here, which were carried out in materials where leak-off is either null or small. We therefore neglect leak-off in this discussion.

As investigated previously [*Garagash and Detournay*, 2000; *Garagash*, 2006], fluid cavitation induced by suction can occur at the fracture tip which results in a region filled with vapour (commonly referred to as a fluid lag) between the fracture tip and the fluid front. Such a fluid lag has been observed experimentally, [*Medlin and Masse*, 1984; *Bunger and Detournay*, 2008] among others. The occurrence of a fluid lag is intrinsically related to a strong pressure gradient within the fracture, such that no fluid lag exists in the limit of large dimensionless toughness. For radial hydraulic fractures, an additional time-scale $t_{om} = \dfrac{E'^2 \mu'}{\sigma_o^3}$ controls the time of coalescence of the fluid and fracture fronts, which occurs for $t \approx t_{om}$ [*Bunger and Detournay*, 2007; *Lecampion and Detournay*, 2007]. The importance of fluid lag therefore vanishes in the case of a large in-situ stress σ_o (e.g. for large depth from the earth surface).

The propagation of a radial hydraulic fracture in an infinite medium (with small leak-off) evolves from a regime where a fluid lag is significant, transitions to the viscosity dominated regime as the fluid lag and fracture tip coalesce and ultimately reaches the toughness regime of propagation at later times. Such an evolution between these different regimes can be grasped via a triangular propagation diagram (face O-M−K in Fig.2a) where each vertex corresponds to a limiting propagation regime: i) O lag dominated, ii) M viscosity dominated, iii) K toughness dominated. The exact nature of the evolution from the O vertex to the K vertex depends on the ratio ψ of the two transition time-scales t_{mk} (from viscosity to toughness regimes) and t_{om} (for the disappearance of the fluid lag):

$$\psi = t_{mk}/t_{om} = \left(\frac{E'^{3/2} Q_o^{1/2} \mu'^{1/2} \sigma_o}{K'^3} \right)^3. \tag{10}$$

In the limit of zero ψ, the toughness regime of propagation is immediately reached (vertex K on Fig.2a), while for large ψ there is a clear distinction between coalescence of the fluid lag and fracture tip (transition from the O to M vertex in Fig. 2a) and transition from viscosity to toughness dominated propagation (vertex M to K).

2.3.2 Initiation from the wellbore - compressibility effects

Initiation from a radial notch at the wellbore wall introduces additional mechanisms that affect hydraulic fracture initiation and the early stage of growth. Prior to fracture initiation, as the wellbore pressure linearly increases under a constant pump injection rate, most of the fluid is stored by compressibility in the injection line/wellbore while a very small amount infiltrates the initial defect. The relative amount of fluid entering
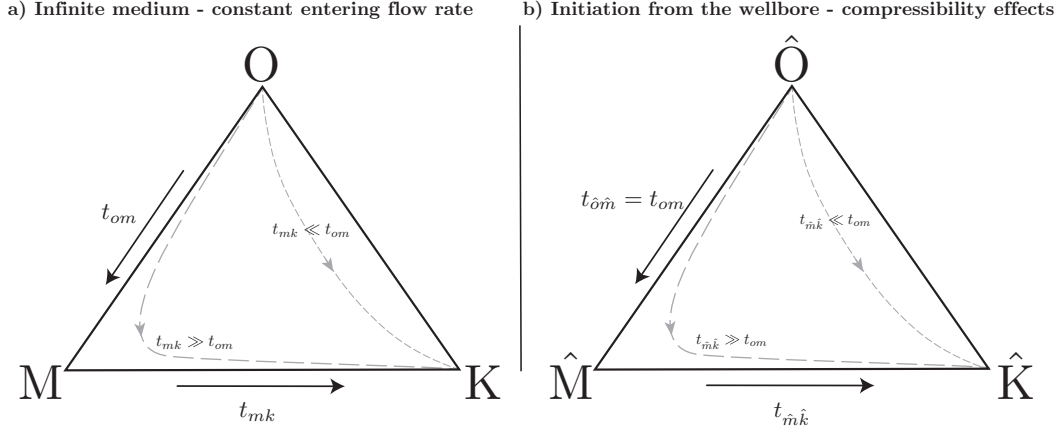
a) Infinite medium - constant entering flow rate

b) Initiation from the wellbore - compressibility effects

O

t_{om}

$t_{mk} \ll t_{om}$

$t_{mk} \gg t_{om}$

M

t_{mk}

K

$\hat{O}$

$t_{\hat{o}\hat{m}} = t_{om}$

$t_{\hat{m}\hat{k}} \ll t_{om}$

$t_{\hat{m}\hat{k}} \gg t_{om}$

$\hat{M}$

$t_{\hat{m}\hat{k}}$

$\hat{K}$

Figure 2. a) A diagram describing the evolution of a radial hydraulic fracture propagating in an infinite elastic impermeable medium driven by a constant entering flow rate (Adapted from *Bunger* [2005]). The hydraulic fracture evolves from the O vertex, where a fluid lag is significant, to the K vertex (toughness dominated regime) if the injection duration is long enough. As the hydraulic fracture develops, if will follow a different trajectory from O to $\hat{K}$ depending on the ratio of time scales: if $t_{mk} \ll t_{om}$ ($\psi \ll 1$) the fracture will follow a path going directly from O to $\hat{K}$, whereas if $t_{mk} \gg t_{om}$ ($\psi \gg 1$) , it will follow a trajectory that will pass through the $\hat{M}$ vertex (viscous dominated regime).

b) When initiating from a wellbore, if the compliance of the injection system is significant, the entering flow rate is not initially constant. A new diagram can be drawn with a similar notation with a $\hat{\ }$ to indicate the compressibility related propagation regimes. The fracture will then start from the $\hat{O}$ vertex (lag-dominated), end in the $\hat{K}$ vertex (toughness dominated), and depending on the ratio of time scales $t_{\hat{m}\hat{k}}/t_{om}$, the fracture will show a path going through a viscosity-dominated regime represented by $\hat{M}$ or not.

the fracture compared to the amount stored in the wellbore depends notably on the fluid viscosity and the injection system compliance. A lower viscosity of the fracturing fluid results in better fluid penetration and a more uniform pressurization of the initial defect compared to larger viscosity for a similar pump rate. As a result the wellbore pressure at which fracture initiation occurs (i.e. the wellbore pressure for which the critical stress intensity factor at the tip of the initial defect is reached) is lower for a low viscosity fluid compared to a more viscous one - as it is easier to initiate an edge fracture uniformly loaded compared to one loaded just at its inlet. This effect was discussed in detail in *Garagash and Detournay* [1997] for a plane-strain configuration although the authors confuse the initiation pressure with the breakdown pressure. The breakdown pressure, which is practically defined as the maximum pressure recorded, can be notably higher than the initiation pressure [*Zhao et al.*, 1996; *Detournay and Carbonell*, 1997]. Indeed, after fracture initiation, fluid penetrates the newly created fracture more or less easily depending on its viscosity and the rate of injection. The wellbore pressure continues to rise up to a maximum (breakdown). The volume of fluid stored by compressibility prior to breakdown is then released and enters the fracture. The flow rate $Q_{in}(t)$ entering the fracture -which is initially zero- thus temporarily exceeds the pump injection rate before tending to the pump rate Q_o at large time. The duration and intensity of this effect depends mainly on fluid viscosity, system compliance and material parameters. For the case of large fluid viscosity/injection rate, it is also important to note that suction occurs within the deformable fracture so that a fluid lag can appear in the defect even prior to fracture initiation [*Garagash and Detournay*, 1997].

At early time, when the injection system compliance has a major effect, the hydraulic fracture initiation and propagation can be shown to start from a regime where a fluid lag is present, transition to a viscosity/compressibility dominated regime and then toward a toughness/compressibility regime. This is somehow similar to the case of propagation in an infinite medium under a constant injection rate. The main difference stems from the fact that the rate entering the fracture is not constant due to the release of fluid stored by compressibility prior to breakdown. This early-time evolution can also be depicted in a triangular diagram (face $\hat{O}$-$\hat{M}$-$\hat{K}$ on Fig.2b) where each vertex corresponds to a limiting propagation regime: i) $\hat{O}$ lag-compressibility dominated, ii) $\hat{M}$ viscosity-compressibility dominated, iii) $\hat{K}$ toughness-compressibility dominated.) The disappearance of the fluid lag is governed by the same time-scale t_{om} as the case of propagation in an infinite medium

under constant injection rate. The transition from the early-time compressibility/viscosity to the early time compressibility/toughness regime is, however, governed by a different time-scale: $t_{\hat{m}\hat{k}} = \dfrac{E'^{5/2}U^{1/2}\mu'}{K'^3}$, which depends notably on the injection system compliance. The wellbore radius a and initial notch length ℓ_o also play a role at early time, especially on the value of the fracture initiation pressure. Their influence is captured by their ratio with a lengthscale $(E'U)^{1/3}$ associated with the release of the fluid stored during the wellbore pressurization prior to initiation: $\mathcal{L} = \ell_o/(E'U)^{1/3}$ and $\mathcal{A} = a/(E'U)^{1/3}$. It is important to note that such a compressibility lengthscale $(E'U)^{1/3}$ is typically larger than both the initial defect length ℓ_o and the wellbore radius a ($\mathcal{L} < 1$ and $\mathcal{A} < 1$) in most practical situations as $E'U \approx E'c_f V_{inj} \approx O(10^{10}Pa) \times O(10^{-10}Pa^{-1}) \times V_{inj} \approx V_{inj}$ (where V_{inj} denotes the volume of the injection line). This indicates that the compressibility effect and the associated release of fluid after breakdown typically dominates the early stage of growth of a radial hydraulic fracture.

2.3.3 Transition towards the infinite medium - constant entering flow rate regime

The complete evolution of a radial hydraulic fracture from initiation to the late stage of propagation can be schematically grasped via the diagram of Fig.3, where the Ô-M̂-K̂ face corresponds to the early-time / compressibility dominated regimes and the O-M-K corresponds to the case of a constant injection in an infinite medium which is reached for time larger than $t_{\hat{m}\hat{k}}$, i.e. after the transient associated with fracture initiation has died out. The transition time-scales between the different propagation regimes are listed in Table 1 (see also Appendix A: for details). We choose to capture the transition from the early time initiation/compressibility to the late time/ constant injection regimes of propagation via the ratio of the corresponding viscosity to toughness transition time-scales:

$$\chi = t_{mk}/t_{\hat{m}\hat{k}} = \frac{E'^4 Q_o^{3/2}\mu'^{3/2}}{K'^6 U^{1/2}} \tag{11}$$

A radial hydraulic fracture always start its life where fluid lag and compressibility dominate (vertex Ô in Fig.3) and evolves ultimately toward the toughness regime of propagation under constant injection rate (vertex K in Fig.3). The complete evolution depends on the ratios of time-scales $\psi = t_{mk}/t_{om}$ and $\chi = t_{mk}/t_{\hat{m}\hat{k}}$ as well as the ratios of characteristic length scales $\mathcal{L} = \ell_o/(E'U)^{1/3}$ and $\mathcal{A} = a/(E'U)^{1/3}$, where $(E'U)^{1/3}$

$$t_{om} \quad = \quad \frac{E'^2 \mu'}{\sigma_o^3}$$

$$t_{mk} \quad = \quad \frac{E'^{13/2} Q_o^{3/2} \mu'^{5/2}}{K'^9}$$

$$t_{\hat{m}\hat{k}} \quad = \quad \frac{E'^{5/2} U^{1/2} \mu'}{K'^3}$$

$$t_{\hat{o}o} \quad = \quad \frac{E'^{1/2} U^{3/4} \mu'^{1/4}}{Q_o^{3/4}} \quad = \quad \chi^{-3/2} t_{mk}$$

$$t_{\hat{m}m} \quad = \quad t_{\hat{o}o} \quad = \quad \chi^{-3/2} t_{mk}$$

$$t_{\hat{k}k} \quad = \quad \frac{K' U^{5/6}}{E'^{1/6} Q_o} \quad = \quad \chi^{-5/2} t_{mk}$$

$$\psi \quad = \quad t_{mk}/t_{om} \quad = \quad \left(\frac{E'^{3/2} Q_o^{1/2} \mu'^{1/2} \sigma_o}{K'^3} \right)^3$$

$$\chi \quad = \quad t_{mk}/t_{\hat{m}\hat{k}} \quad = \quad \frac{E'^4 Q_o^{3/2} \mu'^{3/2}}{K'^6 U^{1/2}}$$

Table 1. **Transition time-scales between limiting propagation regimes as function of problem parameters (e.g. t_{om} represents the transition time between vertex O and vertex M). These time-scales can all be expressed for example via the dimensionless ratios ψ, χ and the characteristic time-scale t_{mk} of transition between viscosity and toughness dominated regime in an infinite medium with a constant entering flow rate.**

is the characteristic lengthscale associated with the released of the volume of fluid stored during wellbore pressurization prior to breakdown.

It is worth noting that, in the limit of an inviscid fluid (zero viscosity) / large toughness, the viscosity-toughness transition time-scales $t_{\hat{m}\hat{k}}$ and t_{mk} tend to zero. In that particular toughness dominated case, the transient effect associated with fracture initiation and breakdown vanishes instantaneously and the propagation takes place directly in the toughnness dominated regime (K vertex in Fig.3). Such a vanishing transient effect is associated with the sudden release of fluid stored by compressibility prior to breakdown and results in an instability (see *Lhomme et al.* [2005] for the complete analytical solution for that limiting case). In all the other cases where fluid viscosity is non-zero, the solution evolves smoothly.
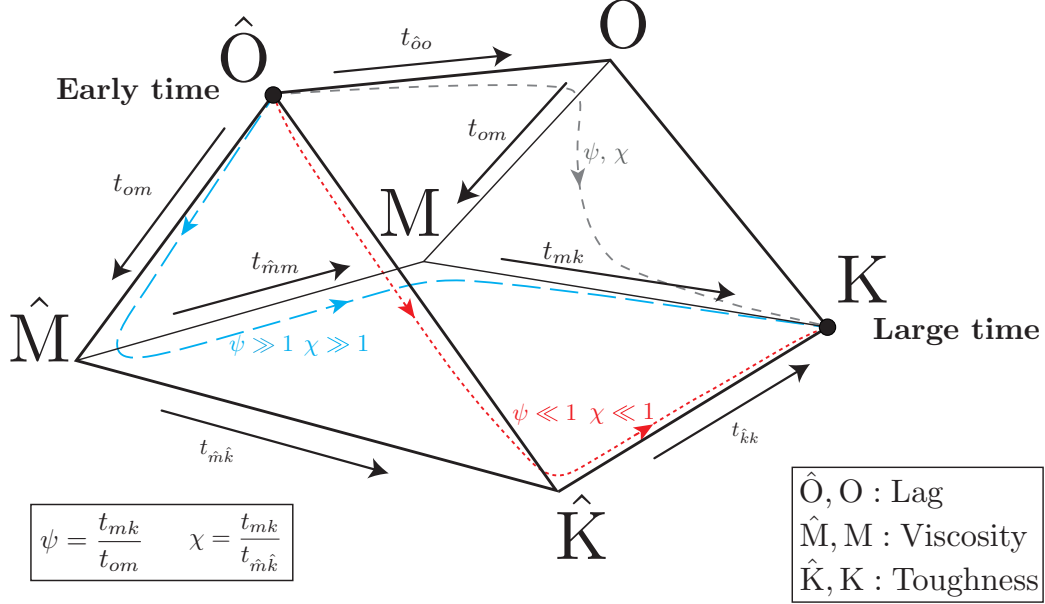
Figure 3. Schematic evolution of the initiation and propagation of radial hydraulic fracture from a wellbore in dimensionless space. Each vertex corresponds to a limiting propagation regime. At early time, the solution is governed by the near-wellbore injection transient ($\hat{O} - \hat{M} - \hat{K}$ face) and evolves toward the constant injection rate propagation in an infinite medium solution at later time ($O - M - K$ face). More precisely, the solution starts in the $\hat{O}$ vertex (fluid lag / compressibility dominated) and ends in the $\hat{K}$ vertex (toughness dominated). Beside the ratio of time-scales $\psi = t_{mk}/t_{om} = \left(\dfrac{E'^{3/2} Q_o^{1/2} \mu'^{1/2} \sigma_o}{K'^3} \right)^3$ and $\chi = t_{mk}/t_{\hat{m}\hat{k}} = \dfrac{E'^4 Q_o^{3/2} \mu'^{3/2}}{K'^6 U^{1/2}}$, the solution also depends on two ratios of length scales $\mathcal{A} = a/(E'U)^{1/3}$ (dimensionless wellbore radius) and $\mathcal{L} = \ell_o/(E'U)^{1/3}$ (dimensionless initial notch).

	Q_o (m^3/s)	μ_f (Pa.s)	χ	ψ	$t_{\hat{m}\hat{k}}$ (s)	t_{mk} (s)
1	10^{-2}	10^{-3}	199	$55.4\,10^3$	0.0209	4.15
2	10^{-5}	1	199	$55.4\,10^3$	20.9	$4.15\,10^3$
3	10^{-5}	10^{-3}	0.0063	1.75	0.0209	$1.3\,10^{-4}$

Table 2. Injection rate, fluid viscosity, dimensionless numbers and characteristic time-scales of the three simulations (the values of the other parameters are listed in the text).

2.4 Illustrating examples

In order to illustrate the different possible trajectories depicted in the schematic propagation diagram of Fig.3, we perform numerical simulations varying the fracturing fluid viscosity and injection rate while keeping the other parameters constant. By doing so, we will span different values of χ, ψ and governing time-scales. For these simulations, we use the following values of parameters: plane strain elastic Young's modulus $E' = 20$GPa, fracture toughness $K_{Ic} = 1$MPa$\sqrt{\text{m}}$, minimum in-situ stress $\sigma_o = 40$MPa, wellbore radius $a = 2.7$ cm, system compliance $U = 10^{-12}$Pa^{-1}m^3 and initial defect length $\ell_o = 2.7$ mm. The dimensionless wellbore radius $\mathcal{A} = 0.1$ and initial defect length $\mathcal{L} = 0.01$ thus do not change in these simulations (their effect on the maximum pressure is discussed in section 4).

We perform three different simulations (denoted 1, 2 and 3). Table 2 summarizes the different injection rates and fluid viscosities for these simulations as well as the resulting dimensionless numbers and characteristic time-scales. The first simulation corresponds to an industrial "field" configuration (e.g. a slickwater hydraulic fracturing reservoir stimulation treatment) with a large injection rate and a water-like fluid viscosity: $Q_o = 10^{-2}$m^3/s, $\mu_f = 10^{-3}$Pa.s. The second and third simulations mimick the case of an injection with a much lower injection rate (e.g. for a diagnostic test) $(Q_o = 10^{-5}$m^3/s). The second simulation is performed with a very viscous fluid $(\mu_f = 1$Pa.s) while the third one uses again a water-like viscosity $(\mu_f = 10^{-3}$Pa.s). Simulations 1 and 2 actually have exactly the same values for the time-scales ratio $\chi = 199$ and $\psi = 55.4\,10^3$: the larger viscosity used in simulation 2 compensates for its smaller injection rate. These simulations (1 and 2) correspond schematically to the blue trajectory depicted in the propagation diagram of Fig.3 where the solution transition to the viscosity dominated regime

after the initiation transient. The third simulation has much lower values for $\chi = 0.0063$ and $\psi = 1.75$ (viscosity of water with a low injection rate). It corresponds schematically to the red trajectory depicted on Fig.3 where the toughness dominated regime is reached directly after initiation - bypassing the viscosity dominated regime.

Figure 4 displays the time evolution of the dimensional and dimensionless (using the toughness-compressibility scaling $\hat{K}$, see Appendix A:) wellbore pressure, entering flow rate and fracture radius for these three cases. It is worthwhile to point out that, when proprely rescaled, simulations 1 and 2 are completely indistinguishable (up to numerical errors). This is expected as they correspond to the exact same values of the dimensionless evolution parameters χ and ψ.

The third simulation exhibits a very different behaviour eventhough it differs from simulation 1 only by its lower injection rate and from simulation 2 only by its lower value of fluid viscosity. The maximum pressure (breakdown) for simulation 3 is close to 10 MPa lower than for simulation 1 and 2 (see Fig.4a). This example highlights the strong effect of fluid viscosity on the early stage transient associated with hydraulic fracture initiation. The release of fluid stored during pressurization occurs over a shorter period for simulation 3 and the overshoot of the entering flow rate above the pump rate is about two orders of magnitude larger (see Fig.4c, d).

The profile of dimensionless net pressure at breakdown (maximum pressure) and at about $5.4\,t_{\hat{m}\hat{k}}$ after breakdown are displayed for these three simulations on Fig.5. The dimensionless values are of course exactly similar for simulations 1 and 2 (same χ and ψ). It is interesting to note that at breakdown, the pressure is already more uniform for simulation 3 while the gradient is steeper for simulations 1 and 2. After the transient associated with fracture initiation has died out (i.e. $\approx 5.4t_{\hat{m}\hat{k}}$ after breakdown), the pressure profiles are very different in the two cases. For large χ and ψ (simulations 1,2), the pressure profile is strongly non-uniform and exhibits a strong gradient at the fracture tip, typical of viscosity dominated fractures [*Detournay*, 2016]. On the contrary, the pressure is nearly uniform for the case of small χ and ψ (simulation 3) which corresponds to the case of a hydraulic fracture propagating in the toughness dominated regime.

Even though we have emphasized for the sake of discussion the case of small versus large viscosity / injection rate (for the same other parameters), the derived scalings do capture the dependency of the evolution of the hydraulic fracture propagation on all
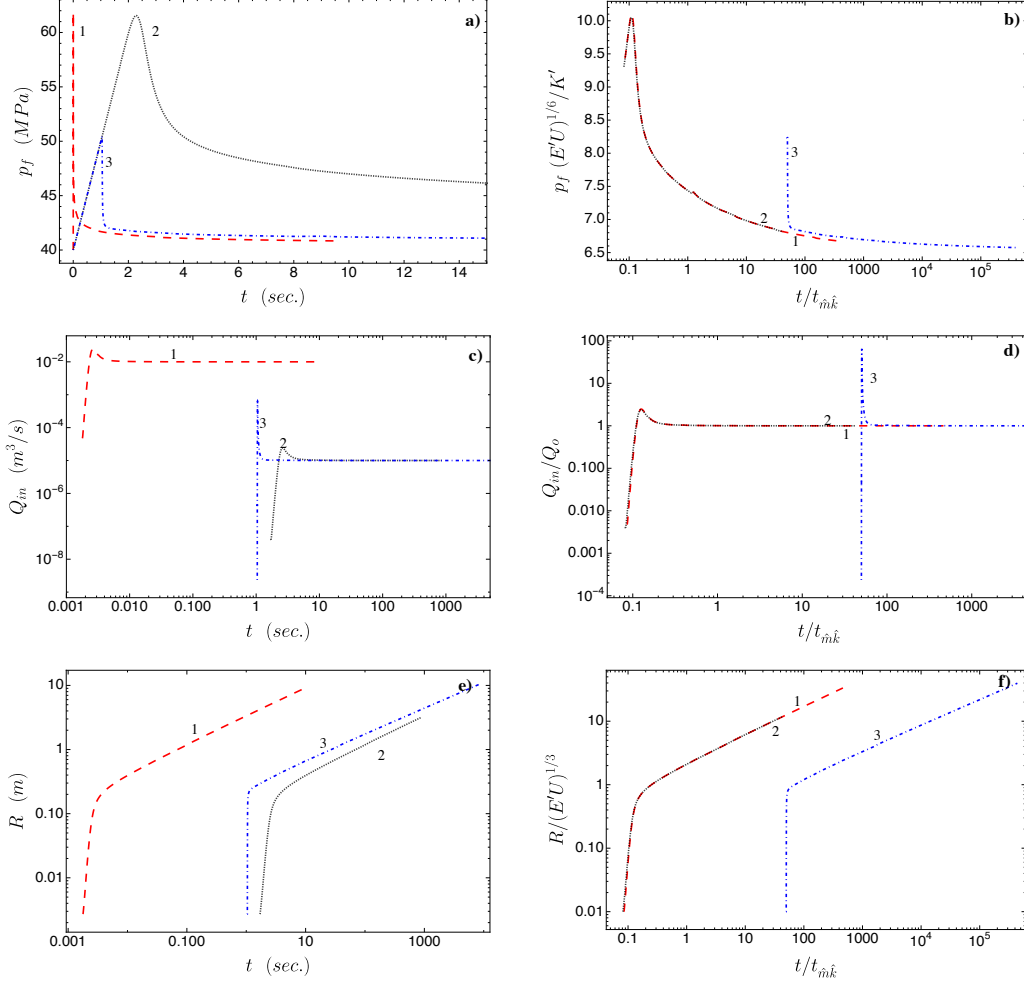
Figure 4. Time evolution of wellbore (fluid) pressure (a-dimensional, b-dimensionless), entering flow rate (c-dimensional, d-dimensionless) and fracture radius (e-dimensional, f-dimensionless) for three simulations with different injection rate and fluid viscosity. Simulations 1 ($Q_o = 10^{-2}\,\mathrm{m^3/s}$, $\mu_f = 10^{-3}\,\mathrm{Pa.s}$) and 2 ($Q_o = 10^{-5}\,\mathrm{m^3/s}$, $\mu_f = 1\,\mathrm{Pa.s}$) have the same dimensionless evolution parameters $\chi = 199$, $\psi = 55.4\,10^3$. These cases are viscosity dominated during the whole duration of the simulation. Simulation 3 ($Q_o = 10^{-5}\,\mathrm{m^3/s}$, $\mu_f = 10^{-3}\,\mathrm{Pa.s}$) has $\chi = 0.0063$, $\psi = 1.75$ and ends up being toughness dominated from early on.
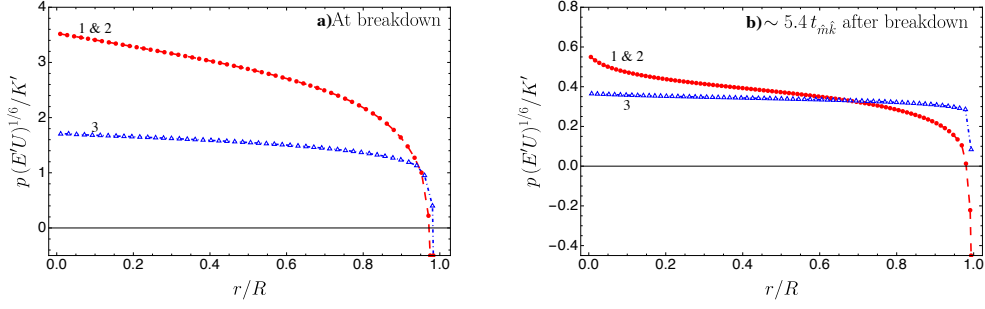
Figure 5. Dimensionless net pressure $(p_f - \sigma_o)$ profiles at breakdown and about $5.4\, t_{\hat{m}\hat{k}}$ after breakdown (after initiation transient) for simulations 1-3. Stronger net pressure gradient are typical of viscosity dominated hydraulic fractures while a uniform net pressure is typical of a toughness dominated propagation.

parameters. Note also that other choices of ratios of time-scales or lengthscales are possible to describe the evolution of the propagation (see Appendix A: for details), but we have found $\chi, \psi, \mathcal{L}$ and $\mathcal{A}$ to be the most convenient in practice. With the understanding of the process obtained from this scaling analysis, one can directly grasp what will govern the system response for a given set of parameters. This is of particular importance when comparing different experiments or when comparing laboratory experiments with field scale operations.

3 Comparisons with experiments

We have selected, among experimental results available in the literature, experiments for which the experimental parameters were clearly known and well constrained (including the length of the initial defect) and where the maximum information on the fracture propagation was available in terms of pressure, width and fracture extent as a function of time. We refrain from changing any parameters to match the measurements: we perform direct comparisons between theoretical predictions and experimental responses. The experiments used here have been performed in two different laboratories (TU Delft and CSIRO) in polyaxial frames on blocks of sizes ranging between 20x20x15 cm and 34x36x40 cm. All experiments reported here have exactly the configuration depicted in Figure 1: radial hydraulic fractures transverse to the wellbore were created.

	Material type	Young's modulus	Poisson's ratio	Fracture Toughness	Carter's leak-off coefficient	Initial defect length
		E (GPa)	ν (-)	K_{Ic} (MPa.$\sqrt{\text{m}}$)	C_l (m/$\sqrt{\text{s}}$)	ℓ_o (mm)
Block4	PMMA	3.3	0.41	1.3	0	1.45
PMGY8	PMMA / glued interface	3.3	0.41	0.38	0	1.5
COV12c	Cement	24.1	0.02	0.5	6.10^{-7}	0.8

Table 3. Material parameters for the different experiments. See the discussion of the different experiments in the text for the details of their independent characterization in each case.

	Block size	Wellbore radius	Confining stress	Fluid viscosity	Injection rate	Pressurization rate	System Compliance
	(cm)	a (mm)	σ_o (MPa)	μ_f (Pa.s)	Q_o (ml/s)	Q_o/U (MPa/s)	U (ml/GPa)
Block4	34-36-40	8.35	0	60	0.0158	0.15	104.7
PMGY8	20-20-15	4	14.5	24.5	0.016	0.113	140.7
COV12c	30-30-30	10	9	130	0.0029	0.019	149

Table 4. Sample configuration and tests parameters for the different experiments. For all tests, the pressurization rate Q_o/U has been obtained from the slope of the pressure-time record during the pressurization phase. The system compliance U is then determined knowing the constant set pump rate Q_o.

	Propagation duration	t_{mk}	$\psi = \frac{t_{mk}}{t_{om}}$	$\chi = \frac{t_{mk}}{t_{\hat{m}\hat{k}}}$	$\mathcal{L} = \ell_o / (E'U)^{1/3}$	$\mathcal{A} = a / (E'U)^{1/3}$
	(s)	(s)				
Block4	500	0.017	$1.6\,10^{-9}$	0.005	0.019	0.11
PMGY8	60	121.9	81.8	2	0.018	0.048
COV12c	1500	$6.9\,10^6$	6997	519	0.005	0.065

Table 5. Experimental fracture propagation duration, viscosity-toughness transition time-scale t_{mk}, time-scale ratios and dimensionless parameters of the different experiments.

The material parameters of the three different experiments are reported in Table 3, while the tests parameters (injection rate, fluid viscosity etc.) are listed in Table 4. For all experiments, we have estimated the total injection system volumetric compressibility U from the linear pressurization phase prior to fracture opening, i.e. dividing the injection rate by the pressurization rate during that period. From the knowledge of this system compliance U and the injection rate, we can perform a numerical derivative of the pressure-time signal recorded during the experiments to obtain an estimate of the fluid flux Q_{in} entering the fracture at any given time, see eq.(9) which expresses the global mass conservation between the pump and the fracture inlet. Such an estimate of Q_{in} is therefore not a direct measurement and may be relatively noisy. The non-monotonic evolution of the entering flow rate is a critical part of the early stage growth as it is directly related to the injection system compliance and is thus worthwhile to compare to the predicted entering flow rate.

Table 5 lists the time-scales and dimensionless parameters introduced previously for the different experiments. The first two experiments (listed as Block 4 and PMGY8) are performed in PMMA, one fracturing intact material and the other fracturing along a pre-existing epoxy glued interface having a lower toughness than PMMA (see *Bunger and Detournay* [2008] for details). The third experiment (named COV12c) was performed in cement and exhibited some leak-off although not enough to be in the leak-off dominated regime.

From Table 5, comparing the test duration with the constant injection viscosity to toughness transition time-scale t_{mk}, we see that most of the fracture propagation will take place in the toughness dominated regime for the first experiment (Block 4) and the viscosity dominated regime for the two others. The effect of fluid lag and system compliance is short-lived for Block 4 experiment ($\psi, \chi \ll 1$), while the other experiments will exhibit some influence of fluid lag/suction as well as a difference between entering flow rate and pump rate in relation to the injection system compressibility.

Comparisons between the results of the numerical model and the experimental data (flux and pressure at the fracture inlet, fracture extension and fracture width or fracture volume) are presented in Figures 7, 8 and 9. For all figures, the experimental data are plotted in blue whereas results from the numerical model are plotted in black. Furthermore, the nominal injection rate and the minimum confining stress are indicated with bold horizontal dashed lines, whereas the initiation time is indicated as a light short-dash vertical line and breakdown is indicated with a light vertical long-dash line.

3.1 Toughness dominated experiment in PMMA (Block 4)

This experiment was originally carried out in 2003 at CSIRO to provide a radial growth data set for comparison with a planar 3D hydraulic fracture model. Block 4 was constructed by gluing machined PMMA sheets, each 40 mm thick, to form a block 340x360x400 mm in size. After machining to size, the block was annealed in an oven at 80°C over a 2 week period, allowing re-polymerization of the PMMA sheets and minizing residual stresses. A radial notch was created in the injection borehole to control the location of fracture initiation. The block was tested in a polyaxial load frame but was subject to biaxial stress with the two horizontal stresses held equal to one another at 2 MPa and the vertical stress set to zero. A video camera was positioned vertically above the block and used to record the fracture growth. Two LVDTs, with sense points anchored just above and below the fracture plane, were used to measure fracture opening at a point located 40 mm from the injection borehole. Elastic properties of the PMMA were measured by uniaxial compression testing carried out on strain gauged prisms cut from the same PMMA sheet as used for block construction. No significant creep was observed during these tests. Fracture toughness was measured using semi-circular bending samples and results were comparable to literature values (see Table 3 for material parameters).
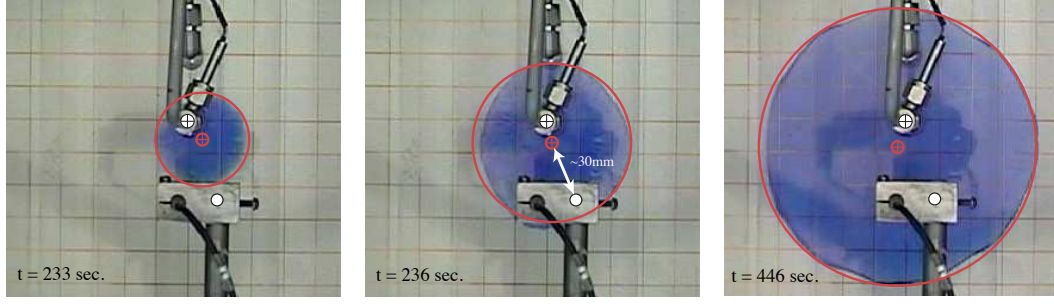
Figure 6. Snapshot of experiment Block 4 in PMMA (top view). The white crossed dot indicates the location of the injection, the red crossed dot the actual center of the fracture (obtained from fitting a circle to the image) and the white dot indicates the location of the LVDT sensor.

The size of the initial notch was measured to be 1.45±0.5mm from a cast of the wellbore after the test. The injection fluid (60 Pa.s silicon oil) was dyed blue and the fracture radius was estimated from the analysis of video recordings of the fracture (see Figure 6). A circle was fitted to the images, allowing the determination of both the fracture radius and the center of the circle. The fracture center is eccentered by about 10 mm, and the location of the LVDTs (displacement sensor) that measured the fracture width is thus 40 mm from the injection point but only 30 mm from the fracture center. The predicted width at both locations is presented in Figure 7. The prediction at 30 mm away from the fracture center proves a better match with the measurements.

This experiment is a case where initiation and breakdown almost perfectly coincide. Initiation – and propagation afterwards - is dominated by toughness. There is a short but very significant entering flux overshoot into the fracture (one order of magnitude above the nominal injection rate) followed by a stable fracture propagation phase under constant flow rate. The match between the model and the measurements, for all the different types of measurements, provides confidence in the ability of the model to capture the relevant physics in that regime.

One may wonder about the effect of the observed translation of the fracture center on the match of the evolution of radius and wellbore pressure. In fact, in this toughness dominated experiment, the fluid pressure is uniform inside the fracture such that moving the location of the injection source has no effect on the fracture propagation. The work of *Gao and Rice* [1987] formally proved this must be the case by showing that a
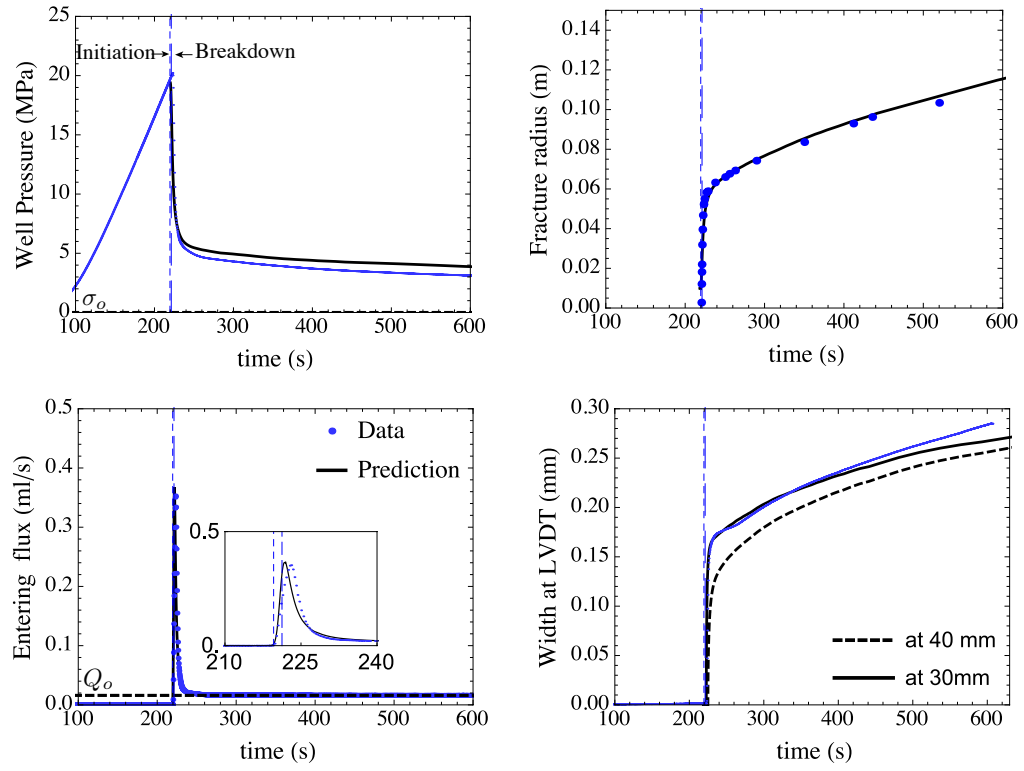
Figure 7. CSIRO Block 4 experiment. Experimental data in blue dots, theoretical prediction in solid black lines.

uniformly pressurized crack will remain circular (i.e. all harmonic perturbations of the circular shape are stable) but will translate due to an instability with respect to location of the crack's centroid. However, the translational instability is not expected for a non-uniform loading, i.e. away from the toughness regime, as shown experimentally by *Bunger* [2005] and predicted by *Gao and Rice* [1987].

3.2 Viscosity dominated experiment in PMMA (PGMY8)

This experiment is reported as experiment PMGY8 in *Bunger and Detournay* [2008]. Contrarily to the previous experiment, the fracture was initiated from a notch along a pre-existing epoxy glued interface. The fracturing fluid was a solution of glucose, water and blue food dye whose viscosity was measured using a capillary viscometer. Taking again advantage of the transparency of PMMA, a photometric method was used to measure both the fracture footprint and the fracture width everywhere across the fracture [*Bunger*, 2006]. Comparison with the model thus encompasses flux entering the fracture, fracture radius, wellbore pressure and fracture width at the wellbore. The results are presented in Figure 8. The fracture toughness of this glued interface was estimated from the tip opening measurements on toughness dominated measurements (see [*Bunger*, 2005] for details).

In this experiment, a needle valve was present in the injection line and pressure was measured both upstream and downstream of this valve. Its influence was modeled by adding a laminar friction pressure drop at the fracture entrance (although there was a small volume downstream of the valve, before the fracture inlet). Such a laminar friction was estimated by taking the pressure drop (between the upstream and the downstream values) at the end of the treatment and dividing it by the nominal injection rate, yielding a value of 2.4MPa (for a rate of 0.016 ml/s). The system compliance was computed from the pressure derivative of the upstream pressure.

Compared with the previous experiment, the flux overshoot is much smaller but lasts longer. Initiation and breakdown pressure are different, especially upstream of the valve. During the experiment, some asymmetry of the fracture geometry was observed, perhaps due to the heterogeneity of the glued interface. The behavior between the experiment and the model starts to diverge around breakdown (especially on the downstream pressure). Nevertheless, the model also captures rather well the behavior dur-
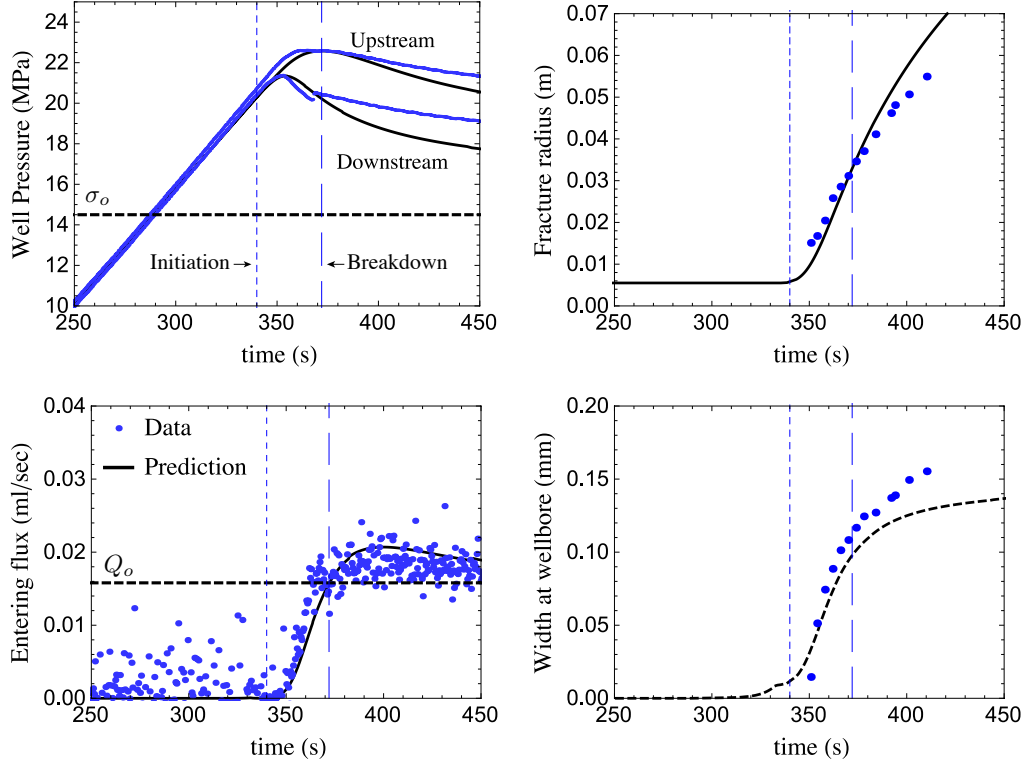
Figure 8. PGMY8 CSIRO glued interface test. Experimental data in blue dots, theoretical prediction in solid black lines.

ing pressurization, initiation and breakdown of the hydraulic fracture for this very different fracture growth regime compared to the previous test.

3.3 Experiment in a cement block (COV12c)

Let us now turn to an experiment in cement, a material that is closer to rocks. Experiment COV12C was carried out at TU Delft and reported as test c12 in *De Pater et al.* [1994]. Evolution of the fracture front was measured using active acoustic scanning. The left and right radius of the fracture front are reported here, and a slight asymmetry develops when the fracture starts to feel the edge of the block. The fracture width at the wellbore was measured from an LVDT located inside the wellbore and the well pressure was measured ahead of the LVDT. The presence of the LVDT in the wellbore introduces a laminar frictional pressure drop in the injection line, estimated at 0.44MPa at the reported injection rate. The elastic properties and fracture toughness of the cement were measured independently from triaxial test (elastic properties) and three point bending

tests. The cement mix used to create the block was also used to create specimen for those tests. The initial notch was casted in place during cement curing using a teflon mold, providing a direct value of the initial defect length (see [*Weijers*, 1995] for details).

The leak-off coefficient C_l was originally estimated by matching the propagation part of the test with a fully coupled radial hydraulic fracturing simulator (see *De Pater et al.* [1996]). In this experiment, the leak-off of the injected fluid into the cement was rather important. At the end of the test, it is estimated from the model that only 45% of the injected volume remains in the fracture. However, leak-off is still less than that required for the fracture to be propagating in the leak-off dominated regime.

Comparison between data and model predictions are displayed in Figure 9. Most of the test period takes place in the transient injection regime during which a variable flux entered the fracture. Moreover, this is the test with the largest difference between the net pressure at initiation (10.5 MPa) and the net pressure at breakdown (17.28 MPa).

This test is yet again in a different regime ($\psi, \chi \gg 1$) compared to the previous tests. The model is able to properly capture the behavior of all parameters during pressurization, initiation and propagation, which hasn't been possible with previous models that did not include the initiation-breakdown phase. A good match was indeed obtained previously on experiments of a similar type (some of these matches can be found in *De Pater et al.* [1996]), but only with the experimental fracture entering flow rate as an input, thus highlighting the importance of taking the injection system dynamics into account during the early stage of hydraulic fracture growth.

4 Discussion and Conclusions

We have compared predictions of hydraulic fracture initiation and propagation with three laboratory experiments performed on low permeability materials (PMMA, cement). These experiments span widely different hydraulic fracture propagation regimes (toughness and viscosity dominated cases, large and small system compliance effects). The good match observed in all cases demonstrates that hydraulic fracture mechanics - as defined by the set of governing equations described here - is predictive, at least for the simple fracture geometry investigated here. It is important to highlight that the theory is able to capture both pressure, fracture width and length evolution with time. This finding provides a high degree of confidence that the relevant physics is properly captured. This
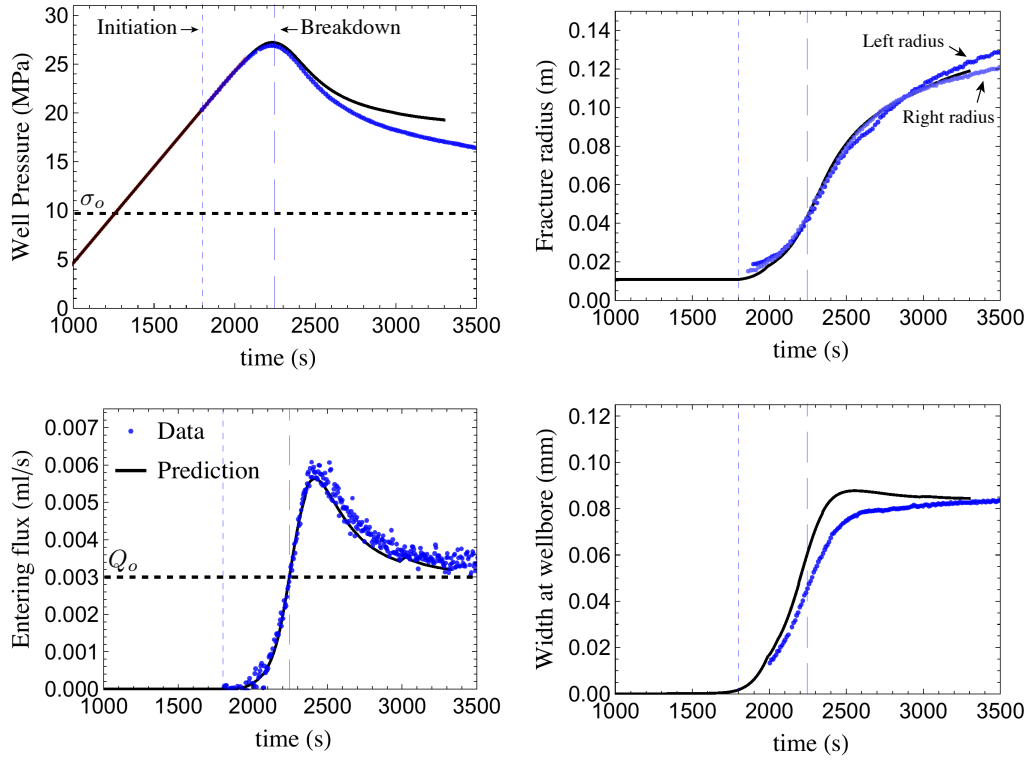
Figure 9. COV21c experiment (performed at TU Delft - *De Pater et al.* [1994]) . Experimental data in blue dots, theoretical prediction in solid black lines.

668 is the first time that such a good comparison has been obtained for the early stage of

669 fracture propagation. The proper prediction of the non-monotonic flux entering the frac-

670 ture due to the release of the volume of fluid stored in the wellbore during the pressur-

671 ization phase appears critical to capture the dynamics of early-stage growth of a hydraulic

672 fracture. Furthermore, linear elastic fracture mechanics, lubrication theory and simple

673 wellbore compressibility appear sufficient to reproduce the experimental data. There is

674 no need, for example, to account for the details of the small-scale yielding at the frac-

675 ture tip (cohesive zone models) for the materials and test conditions investigated here.

676 This may obviously not be the case for coarser grained rocks with respect to the spec-

677 imen size - a topic worth of further investigations. It is important to note that in all ex-

678 periments reported here, hydraulic fracture growth occured in a stable manner. Unsta-

679 ble hydraulic fracture growth may however occur in heterogenous material or when the

680 injection system can not provide enough fluid supply to ensure continuous injection, a

681 topic worth further clarification both experimentally and theoretically. The case of more

682 permeable rocks is also an important topic where more investigations are also needed.

683 In particular, we are not aware of careful experimental measurements of fracture dimen-

684 sions (extent, width) with time in the case of highly permeable rocks where leak off and

685 poroelastic effects are important.

689 Note that the experiments reported here were selected because i) the size of the ini-

690 tial notch (the most difficult parameter to precisely assess) was known with a reason-

691 able degree of accuracy and ii) several complementary quantities (i.e. length, width, pres-

692 sure) were measured. We strongly believe that over-interpretation of any experiment (in

693 the laboratory or in the field) based on a single type of measurement (e.g. pressure) can

694 be strongly misleading. For example, reporting only the breakdown pressure (maximum

695 pressure) appears of very little value.

699 These experiments have highlighted the strong effect associated with viscous flow

700 and hydraulic system compliance at fracture initiation. Notably, the maximum pressure

701 (breakdown pressure) can be significantly higher than the fracture initiation pressure for

702 the case of large viscous effect. The scaling and limiting regimes discussed here provide

703 a quantification of the transient associated with fracture initiation and the early stage

704 of growth. In particular, the relative difference between the maximum and initiation net

705 pressures $\|((p_f^{max} - \sigma_o) - (p_f^{ini} - \sigma_o))/(p_f^{ini} - \sigma_o)\|$ appears to be directly related to the

706 ratio of time-scales $\chi = t_{mk}/t_{\hat{m}\hat{k}} = (E'^4 Q_o^{3/2} \mu'^{3/2})/(K'^6 U^{1/2})$ and to the value of the
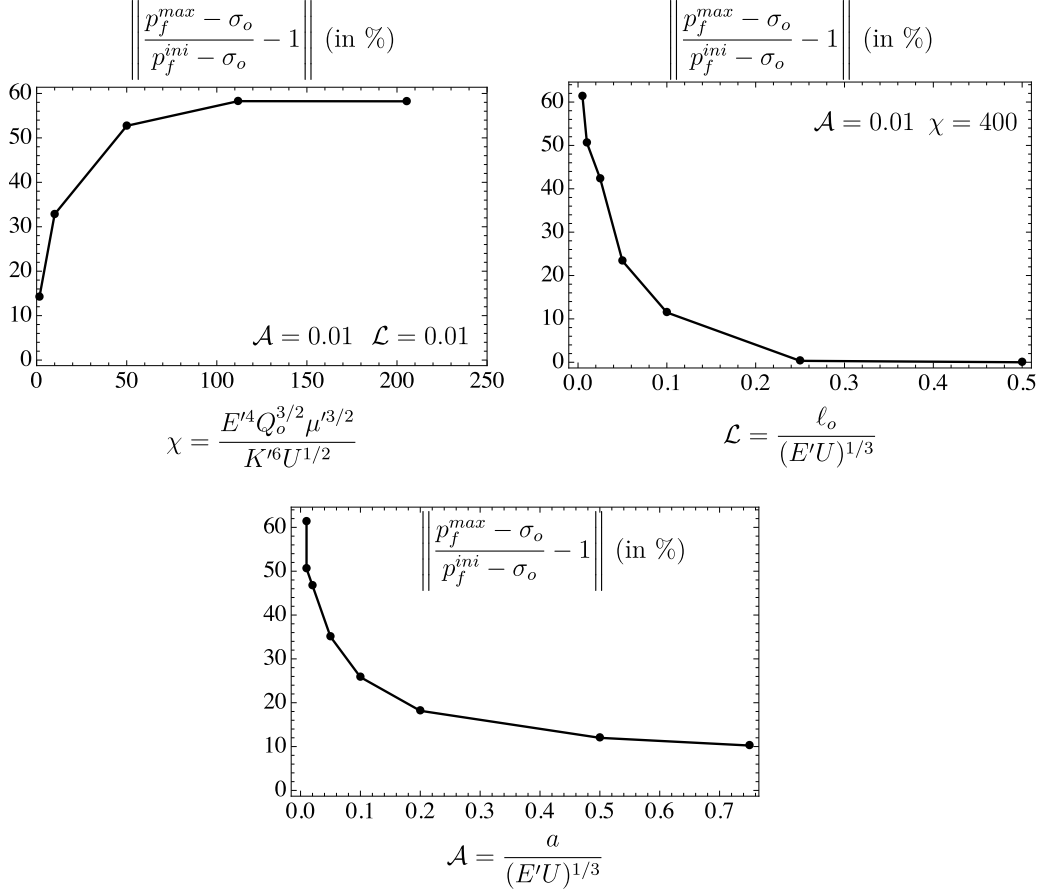
$$\chi = \frac{E'^4 Q_o^{3/2} \mu'^{3/2}}{K'^6 U^{1/2}}$$

$$\mathcal{L} = \frac{\ell_o}{(E'U)^{1/3}}$$

$$\mathcal{A} = \frac{a}{(E'U)^{1/3}}$$

Figure 10. Numerical simulation results illustrating the influence of the dimensionless numbers χ, $\mathcal{L}$ and $\mathcal{A}$ on the relative difference between the maximum (i.e. breakdown) and initiation net pressures: $\left\| (p_f^{max} - \sigma_o)/(p_f^{ini} - \sigma_o) - 1 \right\|$.

	$\left\| \dfrac{p_f^{max} - \sigma_o}{p_f^{ini} - \sigma_o} - 1 \right\|$ (in %)	χ	$\mathcal{L}$	$\mathcal{A}$
Block 4	$\simeq 0\%$	0.005	0.019	0.11
PGMY8	39%	2	0.018	0.048
COV12c	65%	519	0.005	0.065

Table 6. Relative difference between breakdown (maximum) and initiation net pressures $\left\| (p_f^{max} - \sigma_o)/(p_f^{ini} - \sigma_o) - 1 \right\|$. Such a relative difference is related to the ratio of timescales χ and the values of $\mathcal{L}$ and $\mathcal{A}$.

dimensionless initial defect $\mathcal{L} = \ell_o/(E'U)^{1/3}$ and radius $\mathcal{A} = a/(E'U)^{1/3}$. This can be clearly seen from Table 6, as well as from a series of simulations reported in Fig. 10. Fracture initiation and maximum pressures coincide only in the limiting case of small χ. For larger values of χ, the transient effects last longer and the difference between initiation and breakdown pressures is larger. These transients are also a function of the dimensionless ratio of lengthscales associated with the size of the initial notch $\mathcal{L}$ and the wellbore size $\mathcal{A}$: initiation and breakdown pressures are closer to one another for larger values of $\mathcal{L}$ and $\mathcal{A}$ (see Fig. 10).

It is important to bear in mind that in practice (from laboratory experiments to massive hydraulic fracturing treatments in the oil and gas industry) $\mathcal{A}$ and $\mathcal{L}$ are always in the range $[10^{-3} - 10^{-1}]$, whereas χ can vary widely $[10^{-3} - 10^5]$ depending on the fluid and injection rate used. Estimating χ therefore directly allows to know if the initiation and maximum pressure will be significantly different. As an example, let us take the case of a hydraulic fracturing treatment performed in an unconventional reservoir having a plane-strain Young's modulus $E' = 25$GPa and a fracture toughness K_{Ic} of 1.25MPa.$\sqrt{\text{m}}$. Using water as a fracturing fluid ($\mu = 10^{-3}$Pa.s, $c_f = 5 \ 10^{-10}$Pa^{-1}) and a large injection rate ($Q_o = 20$Barrels per minute $= 0.059$m^3/s), for a wellbore length of 3.5 km with an internal diameter of 5" (12.7cm), we obtain a pressurization rate $Q_o/U \approx 7.5$MPa/s. The compressibility fracture lengthscale $(E'U)^{1/3} \approx 6$ meters is much larger than the wellbore radius and initial defect length, i.e. $\mathcal{L} \ll 1$ and $\mathcal{A} \ll 1$. We obtain a value of 38 for χ in that particular case for which the difference between the maximum (breakdown) and initiation pressures is about 40% of the difference between the initiation pressure and the in-situ minimum stress $p_f^{ini} - \sigma_o$ (see Fig. 10). In such large scale fracturing treatments, it is clear that estimating fracture initiation from the pressure record alone (even with a downhole sensor) is nearly impossible due to the intertwined effect of fluid viscosity, system compliance and injection rate discussed above. Initiation pressures are thus often over-estimated as a result.

Although we have presented relatively satisfactory comparisons between theory and experiments for hydraulic fracture initiation, they are restricted to a relatively simple fracture geometry and pure opening mode fractures. The effect of fracture initiation and re-orientation in a complex stress field around a wellbore is known to yield complex fractures, for which theoretical predictions are not yet satisfactory. Such effects were avoided by properly notching the wellbore in the experiments reported here. Investigating ex-

perimentally these effects is possible by playing on the wellbore configuration (see *Weijers* [1995]; *Burghardt et al.* [2015] for examples). Quantitative monitoring of complex non-planar fracture propagation via acoustic or optical methods is certainly not straightforward. Theoretical predictions of mixed modes I, II and III hydraulic fracture propagation may even be more challenging, especially the fracture front segmentation observed experimentally in *Wu et al.* [2007] for example.

Acknowledgments

References

Abbas, S., and B. Lecampion (2013), Initiation and breakdown of an axisymmetric hydraulic fracture transverse to a horizontal wellbore, in *The International Conference for Effective and Sustainable Hydraulic Fracturing, May 20-22, Brisbane, Australia*, Brisbane, Australia.

Abé, H., L. M. Keer, and T. Mura (1976), Growth rate of a penny-shaped crack in hydraulic fracturing offset rocks, *J. Geoph. Res.*, *81*, 6292, doi: doi:10.1029/JB081i035p06292.

Batchelor, G. (1967), *An Introduction to Fluid Dynamics*, Cambridge Univ Press.

Bunger, A. (2005), Near-surface hydraulic fracture, Ph.D. thesis, University of Minnesota.

Bunger, A. (2006), A photometry method for measuring the opening of fluid-filled fractures, *Meas. Sci. Technol.*, *17*, 3237–3244.

Bunger, A., E. Gordeliy, and E. Detournay (2013), Comparison between laboratory experiments and coupled simulations of saucer-shaped hydraulic fractures in homogeneous brittle-elastic solids, *Journal of the Mechanics and Physics of Solids*, *61*(7), 1636–1654.

Bunger, A. P., and E. Detournay (2007), Early-time solution for a radial hydraulic fracture, *Journal of engineering mechanics*, *133*(5), 534–540.

Bunger, A. P., and E. Detournay (2008), Experimental validation of the tip asymptotics for a fluid-driven crack, *J. Mech. Phys. Sol.*, *56*, 3101–3115, doi: 10.1016/j.jmps.2008.08.006.

Bunger, A. P., R. G. Jeffrey, and E. Detournay (2005), Application of scaling laws to laboratory-scale hydraulic fractures, in *Alaska Rocks 2005, The 40th US Symposium on Rock Mechanics (USRMS)*, ARMA/USRMS 05-818.

Burghardt, J., J. Desroches, B. Lecampion, S. Stanchits, A. Surdi, N. Whitney, and M. Houston (2015), Laboratory study of the effect of well orientation, completion design and rock fabric on near-wellbore hydraulic fracture geometry in shales, in *13th ISRM International Symposium on Rock Mechanics*, Montreal.

Cleary, M., and S. Wong (1985), Numerical simulation of unsteady fluid flow and propagation of a circular hydraulic fracture, *International Journal for Numerical and Analytical Methods in Geomechanics*, *9*(1), 1–14.

Cornetti, P., N. Pugno, A. Carpinteri, and D. Taylor (2006), Finite fracture mechanics: A coupled stress and energy failure criterion, *Eng. Frac. Mech.*, *73*, 2021–2033.

De Pater, C., L. Weijers, M. Savic, K. Wolf, P. Van den Hoek, and D. Barr (1994), Experimental study of nonlinear effects in hydraulic fracture propagationw, *SPE Production & Facilities*, *9*(04), 239–246, SPE 25893.

De Pater, H., J. Desroches, J. Groenenboom, and L. Weijers (1996), Physical and numerical modeling of hydraulic fracture closure, *SPE Production & Facilities*, *11*(02), 122–128.

Desroches, J., E. Detournay, B. Lenoach, P. Papanastasiou, J. Pearson, M. Thiercelin, and A. Cheng (1994), The crack tip region in hydraulic fracturing, *Proceedings of the Royal Society of London. Series A: Mathematical and Physical Sciences*, *447*(1929), 39.

Detournay, E. (2004), Propagation regimes of fluid-driven fractures in impermeable rocks, *International Journal of Geomechanics*, *4*(1), 35, doi:10.1061/(ASCE)1532-3641(2004)4:1(35).

Detournay, E. (2016), Mechanics of hydraulic fractures, *Annual Review of Fluid Mechanics*, *48*, 311–339.

Detournay, E., and E. Carbonell (1997), Fracture mechanics analysis of the breakdown process in minifracture or leakoff test, *SPE Production & Facilities*, pp.

195–199.

Detournay, E., and A. Peirce (2014), On the moving boundary conditions for a hydraulic fracture, *Int. J. Eng. Sci.*, *84*, 147–155.

Gao, H., and J. R. Rice (1987), Somewhat circular tensile cracks, *International Journal of Fracture*, *33*(3), 155–174.

Garagash, D. (2006), Propagation of a plane-strain fluid-driven fracture with a fluid lag: early-time solution, *Int. J. Sol. Struct.*, *43*, 5811–5835.

Garagash, D., and E. Detournay (2000), The tip region of a fluid-driven fracture in an elastic medium, *J. Appl. Mech.*, *67*, 183–192.

Garagash, D. I. (2000), Hydraulic fracture propagation in elastic rock with large toughness, in *Rock Around the Rim [Proceedings of the 4th North American Rock Mechanics Symposium, Seattle]*, edited by J. Girard, M. Liebman, C. Breeds, and T. Doe, pp. 221–228, Rotterdam, Balkema.

Garagash, D. I., and E. Detournay (1997), An analysis of the influence of the pressurization rate on the borehole breakdown pressure, *Int. J. Sol. and Struct.*, *34*(24), 3099–3118.

Garagash, D. I., E. Detournay, and J. Adachi (2011), Multiscale tip asymptotics in hydraulic fracture with leak-off, *Journal of Fluid Mechanics*, *669*, 260–297, doi:10.1017/S002211201000501X.

Geertsma, J., and F. De Klerk (1969), A rapid method of predicting width and extent of hydraulically induced fractures, *Journal of Petroleum Technology*, *21*(12), 1571–1581.

Groenenboom, J., and J. T. Fokkema (1998), Monitoring the width of hydraulic fractures with acoustic waves, *Geophysics*, *63*(1), 139–148.

Haimson, B. C., and C. Fairhust (1967), Initiation and extension of hydraulic fractures in rocks, *Soc. Petroleum Eng. J.*, *7*, 310–318.

Hills, D., P. Kelly, D. Dai, and A. Korsunsky (1996), *Solution of Crack Problems: the Distributed Dislocation Technique, Solid Mechanics and its Applications*, vol. 44, Kluwer Academic Publ., Dordrecht.

Howard, G. C., and C. Fast (1957), Optimum fluid characteristics for fracture extension, *Drilling and Production Practice*, pp. 261–270.

Hubbert, M. K., and D. Willis (1957), Mechanics of hydraulic fracturing, *Trans. Am. Inst. Min. Eng.*, *210*, 153–158.

Keer, L. M., V. M. Luk, and J. Freedman (1977), Circumferential edge crack in a cylindrical cavity, *J. Appl. Mech. (ASME)*, *44*(2), 250–253.

Khristianovic, S., and Y. Zheltov (1955), Formation of vertical fractures by means of highly viscous fluids., in *Proc., 4th World Petroleum Congress*, vol. II, pp. 579–586, Rome.

Kovalyshen, Y., and E. Detournay (2013), Fluid-driven fracture in a poroelastic rock, in *ISRM International Conference for Effective and Sustainable Hydraulic Fracturing*, International Society for Rock Mechanics.

Kovalyshen, Y., A. P. Bunger, J. Kear, and D. Kasperczyk (2014), Comparison between ultrasonic and photometric methods for hydraulic fracture laboratory monitoring, *International Journal of Rock Mechanics and Mining Sciences*, *70*, 368–374.

Lai, C., Z. Zheng, E. Dressaire, J. S. Wexler, and H. A. Stone (2015), Experimental study on penny-shaped fluid-driven cracks in an elastic matrix, in *Proc. R. Soc. A*, vol. 471, p. 20150255, The Royal Society.

Lakirouhani, A., E. Detournay, and A. P. Bunger (2016), A reassessment of in-situ stress determination by hydraulic fracturing, *Geophys. J. Int.*

Lecampion, B. (2012a), Modeling size effects associated with tensile fracture initiation from a wellbore, *Int. J. Rock Mech. Min. Sci.*, *56*, 67–76, doi:10.1016/j.ijrmms.2012.07.024.

Lecampion, B. (2012b), Hydraulic fracture initiation from an open-hole: Wellbore size, pressurization rate and fluid-solid coupling effects, in *46th U.S. Rock Mechanics/Geomechanics Symposium*, ARMA 2012-601.

Lecampion, B., and J. Desroches (2015), Simultaneous initiation and growth of multiple radial hydraulic fractures from a horizontal wellbore, *J. Mech. Phys. Sol.*, *82*, 235–258, doi:10.1016/j.jmps.2015.05.010.

Lecampion, B., and E. Detournay (2007), An implicit algorithm for the propagation of a hydraulic fracture with a fluid lag, *Comp. Meth. Appl. Mech. Engng.*, *196*, 4863–4880, doi:10.1016/j.cma.2007.06.011.

Leguillon, D. (2002), Strength or toughness? A criterion for crack onset at a notch, *Eur. J. Mech. A/Solid*, *21*(1), 61–72, doi:10.1016/S0997-7538(01)01184-6.

Lenoach, B. (1995), The crack tip solution for hydraulic fracturing in a permeable solid, *Journal of the Mechanics and Physics of Solids*, *43*(7), 1025–1043.

Lhomme, T., E. Detournay, and R. Jeffrey (2005), Effect of fluid compressibility and borehole radius on the propagation of a fluid-driven fracture, in *Proceedings of 11th International Conference on Fracture*, Turin, Italy.

Lister, J. (1990), Buoyancy-driven fluid fracture: the effects of material toughness and of low-viscosity precursors, *Journal of Fluid Mechanics*, *210*, 263–280.

Lockner, D., and J. Byerlee (1977), Hydrofracture in Weber Sandstone at High Confining Pressure and Differential Stress, *Journal of Geophysical Research*, *82*(14), 2018–2026.

Madyarova, M. (2003), Fluid-driven penny-shaped fracture in permeable rock, Master's thesis, University of Minnesota, Minneapolis, MN, USA.

Medlin, W., and L. Masse (1984), Laboratory experiments in fracture propagation, *SPE Journal*, *24*(03), 256–268.

Peirce, A. P., and E. Detournay (2008), An implicit level set method for modeling hydraulically driven fractures, *Computer Methods in Applied Mechanics and Engineering*, *197*(33-40), 2858–2885, doi:10.1016/j.cma.2008.01.013.

Rice, J. (1968), Mathematical analysis in the mechanics of fracture, in *Fracture: An Advanced Treatise*, vol. 2, edited by H. Liebowitz, chap. 3, pp. 191–311.

Savitski, A., and E. Detournay (2002), Propagation of a penny-shaped fluid-driven fracture in an impermeable rock: asymptotic solutions, *International Journal of Solids and Structures*, *39*(26), 6311–6337, doi:10.1016/S0020-7683(02)00492-4.

Smith, M. B., and C. Montgomery (2015), *Hydraulic Fracturing*, Crc Press.

Spence, D., and P. Sharp (1985), Self-similar solutions for elastohydrodynamic cavity flow, *Proceedings of the Royal Society of London. A. Mathematical and Physical Sciences*, *400*(1819), 289–313.

Stanchits, S., A. Surdi, P. Gathogo, E. Edelman, and R. Suarez-Rivera (2013), Monitoring the early onset of hydraulic fracture initiation by acoustic emission and volumetric deformation measurements, in *47th U.S. Rock Mechanics/Geomechanics Symposium*, American Rock Mechanics Association, ARMA.

Stanchits, S., J. Burghardt, and A. Surdi (2015), Hydraulic fracturing of heterogeneous rock monitored by acoustic emission, *Rock Mechanics and Rock Engineering*, *48*(6), 2513–2527, doi:10.1007/s00603-015-0848-1.

Weijers, L. (1995), The near-wellbore geometry of hydraulic fractures initiated from horizontal and deviated wells, Ph.D. thesis, Delft University of Technology.

Wu, R., L. N. Germanovich, P. E. Van Dyke, and R. P. Lowell (2007), Thermal technique for controlling hydraulic fractures, *Journal of Geophysical Research: Solid Earth*, *112*(B5), 1978–2012.

Zhao, Z., H. Kim, and B. Haimson (1996), Hydraulic fracturing initiation in granite, in *2nd North American Rock Mechanics Symposium*, pp. 1279–1284.

A: Scalings and limiting regimes

In order to obtain a set of meaningful scalings corresponding to the cases where one mechanism dominates over others, following the approach described in *Garagash* [2000]; *Savitski and Detournay* [2002]; *Detournay* [2004]; *Bunger and Detournay* [2007], we introduce characteristic scales (with a subscript $_*$) and express the different problem variables as follows:

$$w = W_*\Omega \qquad p = P_*\Pi \qquad R = L_*\gamma \qquad q = q_*\Psi = \frac{Q_*}{\vartheta L_*}\Psi \qquad R_f = \vartheta L_*\gamma_f$$

We introduce this scaling in the governing equations (1)-(9). We also scale the radial coordinate according to the fluid front location R_f: $\rho = r/R_f$. We directly see that ϑ is a dimensionless number related to the presence of a fluid lag, and $\vartheta = 1$ corresponds to the case where fluid and fracture front coincide. Using such characteristic scales, the governing equations reduce to:

$$\Pi = \mathcal{G}_e \int_{\mathcal{G}_a/\vartheta}^{\gamma/\vartheta} \Omega \mathrm{d}\rho' \tag{A.1}$$

$$t\frac{\partial\Omega}{\partial t} + \mathcal{G}_v \frac{1}{\rho}\frac{\partial}{\partial\rho}\rho\Psi + \frac{\mathcal{G}_c}{\sqrt{1 - t_o(\rho)/t}} = 0 \qquad \text{for } \rho \in [\mathcal{G}_a, 1] \tag{A.2}$$

$$\Psi = -\frac{\Omega^3}{\mathcal{G}_m}\frac{\partial\Pi}{\partial\rho} \qquad \text{for } \rho \in [\mathcal{G}_a, 1]$$

$$\Pi = -\mathcal{G}_\sigma \qquad \text{for } \rho \in [1, \gamma/\vartheta]$$

$$\Omega \sim \mathcal{G}_k\sqrt{\gamma - \rho/\vartheta} \qquad \text{for } \gamma - \rho/\vartheta \ll 1$$

$$2\pi(\mathcal{G}_a/\vartheta)\Psi(\rho = \mathcal{G}_a/\vartheta) = \mathcal{G}_q - \mathcal{G}_u t\frac{\partial\Pi}{\partial t}$$

The different dimensionless groups denoted $\mathcal{G}$ entering the scaled system of equations are related to distinct different mechanisms:

- $\mathcal{G}_e = \frac{W_* E'}{\vartheta L_* P_*}$ - relates net pressure and fracture opening in the elastic equation
- $\mathcal{G}_v = \frac{Q_* t}{W_* \vartheta^2 L_*^2}$ - relates to the volume stored in the fracture

922 • $\mathcal{G}_c = \frac{C'\sqrt{t}}{W_*}$ - relates to the volume "leaked-off" the fracture faces into the rock

923 • $\mathcal{G}_m = \frac{\mu' Q_*}{W_*^3 P_*}$ - relates to the viscous resistance to flow inside the fracture

924 • $\mathcal{G}_k = \frac{K' L_*^{1/2}}{E' W_*}$ - relates to the fracture propagation condition (dimensionless tough-

925   ness)

926 • $\mathcal{G}_q = \frac{Q_o}{Q_*}$ - relates to the injection rate

927 • $\mathcal{G}_u = \frac{U P_*}{Q_* t}$ - relates to the volume stored in the wellbore during pressurization

928   (i.e. when little fluid is entering the fracture)

929 • $\mathcal{G}_a = a/(\vartheta L_*)$ - is a dimensionless wellbore radius

930 • $\mathcal{G}_\sigma = \sigma_o/P_*$ - is a dimensionless confining stress

931 • $\mathcal{G}_{\ell_o} = \ell_o/(\vartheta L_*)$ - is a dimensionless initial notch

932 • and ϑ relates to the presence of a fluid lag.

933 Putting five of these dimensionless groups to unity enables to solve for the characteris-

934 tic scales L_*, W_*, P_* and Q_* as well as the characteristic ratio between fluid front and

935 fracture front ϑ as function of problem parameters (E', μ' etc.) and time. Different choices

936 are possible therefore defining different scalings. The selected choice of dimensionless groups

937 for the different scalings discussed herein is presented in Fig.A.1. In a given scaling, the

938 dimensionless solution $\mathcal{F} = \{\gamma, \gamma_f, \Omega, \Pi, \Psi\}$ depends on the remaining dimensionless

939 numbers (i.e. not set to unity) and the spatial coordinate $\rho = r/R(t)$ (for opening, pres-

940 sure and fluid flux profiles). In particular, we want to obtain dimensionless opening Ω

941 and pressure Π of similar order and therefore always set the dimensionless number en-

942 tering the elasticity equation $\mathcal{G}_e$ to unity. We are here interested in the case of 'tight' rocks

943 and anticipate negligible leak-off ($\mathcal{G}_c \ll 1$) - i.e. we do not seek leak-off dominated scal-

944 ings (see *Madyarova* [2003] for that case).

945   It is important to remember that we can always switch back and forth between scal-

946 ings (see Supplementary Materials for a Mathematica code deriving all the scalings dis-

947 cussed here and their relationship). We can also define transition time-scales between

948 two scalings and express the dimensionless numbers governing the fracture propagation

949 via these time-scales. We now discuss the salient features of the different initiation/propagation

950 regimes that can be obtained from their scalings.

Infinite medium - constant injection scalings

The case of a radial hydraulic fracture propagating in an infinite medium under constant injection rate and negligible leak-off corresponds to $\mathcal{G}_e = \mathcal{G}_v = \mathcal{G}_q = 1$ (i.e. all the injected volume remaining in the fracture and the inlet flow rate maintained constant). Depending on the relative importance of toughness and viscosity dissipation, a viscosity (M, i.e. $\mathcal{G}_m = 1$) or a toughness (K, i.e. $\mathcal{G}_k = 1$) scaling is relevant in the absence of fluid lag ($\vartheta = 1$). The hydraulic fracture then evolves from the viscosity dominated regime toward the toughness dominated regime at large time. This can be physically grasped by the fact that as the fracture perimeter increases, more and more fracture energy is needed to drive the fracture further, while the viscous drop is dominant for small fracture (with narrow opening) but is less important for large fractures that have a wider opening (see also Table A.2 where we can see that the dimensionless toughness increases with time). The transition from the viscosity (M) to the toughness (K) propagation regime is characterized by the following time scale t_{mk}:

$$t_{mk} = \frac{E'^{13/2} Q_o^{3/2} \mu'^{5/2}}{K'^9}$$

which corresponds to the time where the dimensionless toughness in the M-scaling is equal to unity. The viscosity and toughness scalings -originally derived in *Savitski and Detournay* [2002]- capture the hydraulic fracture propagation once the transient effects associated with fracture initiation from the wellbore becomes negligible. It is interesting to note that the dimensionless injection system compliance $\mathcal{G}_U$ and wellbore radius $\mathcal{G}_a$ both decrease with time in such scalings - i.e. their effects become less and less important as the propagation progresses (see Table A.2). It is also worth recalling that the complete transition from the viscosity to the toughness dominated regime occurs for $\mathcal{G}_k \sim 3.5$ (in the viscosity scaling), which corresponds to $t/t_{mk} \sim 8 \times 10^4$ (see *Savitski and Detournay* [2002] for details).

When the fluid is allowed to lag behind the fracture front, a lag-scaling (O) can be obtained ($\mathcal{G}_e = \mathcal{G}_v = \mathcal{G}_q = \mathcal{G}_m = \mathcal{G}_k = 1$). It can be shown (see *Lecampion and Detournay* [2007]; *Bunger and Detournay* [2007]; *Garagash* [2006]) that the effect of the fluid lag is important during the early stage of the fracture propagation. The hydraulic fracture then evolves from a lag-dominated regime at early-time to the toughness dominated regime at large time, possibly spending a large amount of time in the viscous dominated regime. The hydraulic fracture propagation is controlled by the ratio ψ of the timescales

of transition from viscosity to toughness t_{mk} over the transition from lag to viscosity dominated regimes t_{om}:

$$\psi = \frac{t_{mk}}{t_{om}} = \left(\frac{E'^{3/2}Q_o^{1/2}\mu'^{1/2}\sigma_o}{K'^3} \right)^3$$

where the timescale associated with the disappearance of the fluid lag t_{om} is given by:

$$t_{om} = \frac{E'^2\mu'}{\sigma_o^3}$$

It is important to note that for the case where $\psi \to 0$, the fluid lag disappears.

Early-time/Initiation scalings

At or just after fracture initiation, it seems natural to choose the initial defect length as the dominating lengthscale $L_* = \ell_o$. Moreover, the volume stored by compressibility in the injection line remains larger than the volume stored in the fracture. The flow rate entering the fracture is thus not constant in that regime. We therefore set $\mathcal{G}_e = \mathcal{G}_{\ell_o} = \mathcal{G}_u = 1$. Similarly to the case of constant injection rate, the hydraulic fracture will evolve from a lag-dominated regime ($\breve{O}$) at early time to a toughness dominated regime ($\breve{K}$) via a viscosity dominated regime ($\breve{M}$). Interestingly, the disappearance of the lag is governed by the same time-scale t_{om} as for the case of constant injection rate in an infinite medium. The transition from the viscosity to toughness regime in such an initiation regime is captured by the timescale $t_{\breve{m}\breve{k}}$:

$$t_{\breve{m}\breve{k}} = \frac{E'U\mu'}{K'^3\ell_o^{3/2}}$$

Another choice of length-scale also makes sense at early time: $L_* = (E'U)^{1/3}$. This lengthscale corresponds to a hydraulic fracture with a volume of the same order as the volume of fluid stored by compressibility in the wellbore during the pressurization phase prior to breakdown. The volume stored during pressurization scales as $U \times \Delta p$, while the fracture volume scales as $L_*^3\Delta p/E'$ (from elasticity), which gives $L_* = (E'U)^{1/3}$. This type of scaling corresponds to $\mathcal{G}_e = \mathcal{G}_v = \mathcal{G}_u = 1$. We will refer to the corresponding lag, viscosity and toughness scalings as compressibility scalings (i.e. in relation to the injection system compliance).

The relative ratio of these two lengthscales $\mathcal{L} = \ell_o/(E'U)^{1/3}$ controls which scalings (initiation or compressibility lengthscale dominated) is more representative for a particular case. These early time scalings either based on the initial defect or compressibil-

1008   ity lengthscales are intrinsically similar: only the ratio $\mathcal{L}$ enters the correspondance be-

1009   tween these two types of early-time scalings. In most cases, the compressibility length-

1010   scale is actually much larger than the initial defect length ($\mathcal{L} \ll 1$) such that the com-

1011   pressibility based scaling is more appropriate - i.e. at early time, after initiation, the hy-

1012   draulic fracture propagation is mostly governed by the release of fluid stored by compress-

1013   ibility in the wellbore during pressurization. The timescale associated with the transi-

1014   tion from viscosity to toughness dominated propagation in such compressibility scaling

1015   is given by

$$t_{\hat{m}\hat{k}} = \frac{E'^{5/2}U^{1/2}\mu'}{K'^3} = \mathcal{L}^{3/2}\,t_{\check{m}\check{k}}$$

1016   It is worthwhile to note that in these early-time scalings, the dimensionless injection rate

1017 $\mathcal{G}_q$ increases with time, highlighting the transition from negligible fluid flow entering the

1018   fracture prior to its initiation (i.e. when the well is just being pressurized) to the con-

1019   stant pump rate value at large time (see Table A.2).

1020   ### Transition from initiation to constant injection

1021   The transition from the early-time propagation to the large time constant injec-

1022   tion regimes can be grasped by the transition time-scales $t_{\hat{k}k}$ from the compressibility

1023   toughness scaling $\hat{K}$ to the large time constant injection toughness regime K, or similarly

1024 $t_{\hat{m}m}$ or $t_{\hat{o}o}$. In fact, these different timescales are all related (see Table A.3) and can be

1025   expressed via the ratio of transition time-scales between viscosity and toughness regimes

1026   in the constant injection and compressibility scalings:

$$\chi = \frac{t_{mk}}{t_{\hat{m}\hat{k}}} = \frac{E'^4 Q_o^{3/2}\mu'^{3/2}}{K'^6 U^{1/2}}$$

1028   From the different scalings (Tables A.1 and A.2), we see that for a given configu-

1029   ration, the hydraulic fracture will start its life from the initial lag-compressibility regime

1030   ($\hat{O}$) and evolves toward the constant-injection/infinite medium toughness regime at large

1031   time. The ratio of time-scales ψ and χ governs the trajectory of the hydraulic fracture

1032   between these early and late time regimes.

1038   ### Negligible effect of fluid compressibility inside the fracture

1039   The effect of fluid compressibility c_f in the fluid flow inside the fracture yields an

1040   additional term in the dimensionless continuity equation (A.2): $c_f P_* t\Omega\dfrac{\partial\Pi}{\partial t}$. In all the

Scaling	L_*	ϑ	W_*	P_*	Q_*
Ǒ	$\dfrac{E'^{4/3}\ell_o^2\mu'^{2/3}}{K'^2 t^{2/3}}$	$\dfrac{K'^2 t^{2/3}}{E'^{4/3}\ell_o\mu'^{2/3}}$	$\dfrac{\ell_o\mu'^{1/3}}{E'^{1/3}t^{1/3}}$	$\dfrac{E'^{2/3}\mu'^{1/3}}{t^{1/3}}$	$\dfrac{\ell_o^3\mu'^{1/3}}{E'^{1/3}t^{4/3}}$
M̌	ℓ_o	1	$\dfrac{\ell_o\mu'^{1/3}}{E'^{1/3}t^{1/3}}$	$\dfrac{E'^{2/3}\mu'^{1/3}}{t^{1/3}}$	$\dfrac{\ell_o^3\mu'^{1/3}}{E'^{1/3}t^{4/3}}$
Ǩ	ℓ_o	1	$\dfrac{K'\ell_o^{1/2}}{E'}$	$\dfrac{K'}{\ell_o^{1/2}}$	$\dfrac{K'\ell_o^{5/2}}{E't}$
Ô	$\dfrac{E'^2 U^{2/3}\mu'^{2/3}}{K'^2 t^{2/3}}$	$\dfrac{K'^2 t^{2/3}}{E'^{5/3}U^{1/3}\mu'^{2/3}}$	$\dfrac{U^{1/3}\mu'^{1/3}}{t^{1/3}}$	$\dfrac{E'^{2/3}\mu'^{1/3}}{t^{1/3}}$	$\dfrac{E'^{2/3}U\mu'^{1/3}}{t^{4/3}}$
M̂	$(E'U)^{1/3}$	1	$\dfrac{U^{1/3}\mu'^{1/3}}{t^{1/3}}$	$\dfrac{E'^{2/3}\mu'^{1/3}}{t^{1/3}}$	$\dfrac{E'^{2/3}U\mu'^{1/3}}{t^{4/3}}$
K̂	$(E'U)^{1/3}$	1	$\dfrac{K'U^{1/6}}{E'^{5/6}}$	$\dfrac{K'}{E'^{1/6}U^{1/6}}$	$\dfrac{K'U^{5/6}}{E'^{1/6}t}$
O	$\dfrac{E'^{14/9}Q_o^{2/3}\mu'^{4/9}t^{2/9}}{K'^2}$	$\dfrac{K'^2 t^{2/9}}{E'^{13/9}Q_o^{1/3}\mu'^{5/9}}$	$\dfrac{\mu'^{2/9}Q_o^{1/3}t^{1/9}}{E'^{2/9}}$	$\dfrac{E'^{2/3}\mu'^{1/3}}{t^{1/3}}$	Q_o
M	$\dfrac{E'^{1/9}Q_o^{1/3}t^{4/9}}{\mu'^{1/9}}$	1	$\dfrac{\mu'^{2/9}Q_o^{1/3}t^{1/3}}{E'^{2/9}}$	$\dfrac{E'^{2/3}\mu'^{1/3}}{t^{1/3}}$	Q_o
K	$\dfrac{E'^{2/5}Q_o^{2/5}t^{2/5}}{K'^{2/5}}$	1	$\dfrac{K'^{4/5}Q_o^{1/5}t^{1/5}}{E'^{4/5}}$	$\dfrac{K'^{6/5}}{E'^{1/5}Q_o^{1/5}t^{1/5}}$	Q_o

Table A.1.   Characteristic scales in the different scalings.

- O constant injection-lag scaling $\mathcal{G}_e = \mathcal{G}_v = \mathcal{G}_q = \mathcal{G}_m = \mathcal{G}_k = 1$

- M constant injection - viscosity scaling $\mathcal{G}_e = \mathcal{G}_v = \mathcal{G}_q = \mathcal{G}_m = \vartheta = 1$

- K constant injection - toughness scaling $\mathcal{G}_e = \mathcal{G}_v = \mathcal{G}_q = \mathcal{G}_k = \vartheta = 1$

- Ǒ initial defect - lag scaling $\mathcal{G}_e = \mathcal{G}_v = \mathcal{G}_{\ell_o} = \mathcal{G}_m = \mathcal{G}_k = 1$

- M̌ initial defect - viscosity scaling $\mathcal{G}_e = \mathcal{G}_v = \mathcal{G}_{\ell_o} = \mathcal{G}_m = \vartheta = 1$

- Ǩ initial defect - viscosity scaling $\mathcal{G}_e = \mathcal{G}_v = \mathcal{G}_{\ell_o} = \mathcal{G}_k = \vartheta = 1$

- Ô initial compressibility - lag scaling $\mathcal{G}_e = \mathcal{G}_v = \mathcal{G}_u = \mathcal{G}_m = \mathcal{G}_k = 1$

- M̂ initial compressibility - viscosity scaling $\mathcal{G}_e = \mathcal{G}_v = \mathcal{G}_u = \mathcal{G}_m = \vartheta = 1$

- K̂ initial compressibility - viscosity scaling $\mathcal{G}_e = \mathcal{G}_v = \mathcal{G}_u = \mathcal{G}_k = \vartheta = 1$

Figure A.1.   Definition of the different scalings used in terms of dimensionless groups.

	ϑ	$\mathcal{G}_k$	$\mathcal{G}_m$	$\mathcal{G}_\sigma$
Ǒ	$\left(\frac{t}{t_{\hat{m}\hat{k}}}\right)^{2/3}\mathcal{L}^{-1}$	1	1	$\left(\frac{t}{t_{om}}\right)^{1/3}$
M̌	1	$\left(\frac{t}{t_{\hat{m}\hat{k}}}\right)^{1/3}\mathcal{L}^{-1/2}$	1	$\left(\frac{t}{t_{om}}\right)^{1/3}$
Ǩ	1	1	$\left(\frac{t}{t_{\hat{m}\hat{k}}}\right)^{-1}\mathcal{L}^{3/2}$	$\psi^{1/3}\chi^{-1/3}\mathcal{L}^{1/2}$
Ô	$\left(\frac{t}{t_{\hat{m}\hat{k}}}\right)^{2/3}$	1	1	$\left(\frac{t}{t_{om}}\right)^{1/3}$
M̂	1	$\left(\frac{t}{t_{\hat{m}\hat{k}}}\right)^{1/3}$	1	$\left(\frac{t}{t_{om}}\right)^{1/3}$
K̂	1	1	$\left(\frac{t}{t_{\hat{m}\hat{k}}}\right)^{-1}$	$\psi^{1/3}\chi^{-1/3}$
O	$\left(\frac{t}{t_{mk}}\right)^{2/9}$	1	1	$\left(\frac{t}{t_{om}}\right)^{1/3}$
M	1	$\left(\frac{t}{t_{mk}}\right)^{1/9}$	1	$\left(\frac{t}{t_{om}}\right)^{1/3}$
K	1	1	$\left(\frac{t}{t_{mk}}\right)^{-2/5}$	$\left(\frac{t}{t_{om}}\right)^{1/5}\psi^{2/15}$

	$\mathcal{G}_u$	$\mathcal{G}_q$	$\mathcal{G}_{\ell_o}$	$\mathcal{G}_a$
Ǒ	1	$\left(\frac{t}{t_{\hat{m}\hat{k}}}\right)^{4/3}\chi^{2/3}\mathcal{L}^{-3}$	1	$\mathcal{A}\mathcal{L}^{-1}$
M̌	1	$\left(\frac{t}{t_{\hat{m}\hat{k}}}\right)^{4/3}\chi^{2/3}\mathcal{L}^{-3}$	1	$\mathcal{A}\mathcal{L}^{-1}$
Ǩ	1	$\left(\frac{t}{t_{\hat{m}\hat{k}}}\right)\chi^{2/3}\mathcal{L}^{-5/2}$	1	$\mathcal{A}\mathcal{L}^{-1}$
Ô	1	$\left(\frac{t}{t_{\hat{m}\hat{k}}}\right)^{4/3}\chi^{2/3}$	$\mathcal{L}$	$\mathcal{A}$
M̂	1	$\left(\frac{t}{t_{\hat{m}\hat{k}}}\right)^{4/3}\chi^{2/3}$	$\mathcal{L}$	$\mathcal{A}$
K̂	1	$\left(\frac{t}{t_{\hat{m}\hat{k}}}\right)\chi^{2/3}$	$\mathcal{L}$	$\mathcal{A}$
O	$\left(\frac{t}{t_{mk}}\right)^{-4/3}\chi^{-2}$	1	$\left(\frac{t}{t_{mk}}\right)^{-4/9}\chi^{-2/3}\mathcal{L}$	$\left(\frac{t}{t_{mk}}\right)^{-4/9}\chi^{-2/3}\mathcal{A}$
M	$\left(\frac{t}{t_{mk}}\right)^{-4/3}\chi^{-2}$	1	$\left(\frac{t}{t_{mk}}\right)^{-4/9}\chi^{-2/3}\mathcal{L}$	$\left(\frac{t}{t_{mk}}\right)^{-4/9}\chi^{-2/3}\mathcal{A}$
K	$\left(\frac{t}{t_{mk}}\right)^{-6/5}\chi^{-2}$	1	$\left(\frac{t}{t_{mk}}\right)^{-2/5}\chi^{-2/3}\mathcal{L}$	$\left(\frac{t}{t_{mk}}\right)^{-2/5}\chi^{-2/3}\mathcal{A}$

Table A.2. Dimensionless numbers governing fracture propagation in the different scalings, expressed as functions of the characteristic transition time-scales.

$t_{\hat{k}k}$	$t_{\hat{m}\hat{k}}^{5/3}t_{mk}^{-2/3} = \chi^{-2/3}t_{\hat{m}\hat{k}} = \chi^{-5/3}t_{mk}$
$t_{\hat{m}m}$	$t_{\hat{m}\hat{k}}^{3/2}t_{mk}^{-1/2} = \chi^{-1/2}t_{\hat{m}\hat{k}} = \chi^{-3/2}t_{mk}$
$t_{\hat{o}o}$	$t_{\hat{m}m} = \chi^{-1/2}t_{\hat{m}\hat{k}} = \chi^{-3/2}t_{mk}$

Table A.3. Correspondence between transition time-scales from early time to late time propagation.

scalings derived, the dimensionless opening and net pressure are of similar order, such that the intensity of the effect of fluid compressibility is directly related to the dimensionless quantity $\mathcal{G}_f = c_f P_*$. From the expression of P_* in the different scalings, we see that the effect of fluid compressibility will always decrease with time, except for toughness-based scalings where that effect is constant. Taking a fluid compressibility $c_f = 5 \times 10^{-10}$ representative of liquid water, using the parameters of the experiments discussed in this paper (Tables 3-4), we can see that $c_f P_*$ is of the order $\mathrm{O}(10^{-3})$ in the toughness-based scalings and becomes negligible for times larger than micro-seconds in all the other scalings. The effect of fluid compressibility on the fluid flow inside the fracture can thus be neglected compared to the elastic fracture compliance in the fluid mass conservation equation (2). As shown in this paper, the effect of fluid compressibility in the injection system is, however, not negligible at early time.

B: Nomenclature

- a wellbore radius $[m]$
- c_f fluid compressibility $[Pa^{-1}]$
- g_l leak-off rate from the fractures faces - per fracture area $[m/s]$
- ℓ_o initial notch length $[m]$
- p normal net loading on the fracture face $[Pa]$
- p_{cav} fluid cavitation pressure $[Pa]$
- p_f fluid pressure $[Pa]$
- p_{ini} fracture initiation pressure $[Pa]$
- p_{max} maximum fluid pressure (breakdown) during a test $[Pa]$
- q fluid flux per unit length $[m^2/s]$
- r, r' radial coordinate originating from the wellbore axis $[m]$

- t time $[s]$
- $t_o(r)$ time at which fluid reaches point of coordinate r $[s]$
- t_{mk} transition time between late time viscosity and late time toughness dominated regimes $[s]$
- $t_{\hat{m}\hat{k}}$ transition time between early time viscosity and early time toughness dominated regimes $[s]$
- t_{om} characteristic time related to the coalescence of the fluid lag and the fracture tip $[s]$
- w fracture width $[m]$
- C' total leak-off coefficient - $C' = 2C_L$ $[m.s^{-0.5}]$
- C_L Carter's leak-off coefficient $[m.s^{-0.5}]$
- E Young's modulus $[Pa]$
- E' plane strain Young's modulus - $E' = E/(1 - \nu^2)$ $[Pa]$
- K' reduced fracture toughness - $K' = \sqrt{\dfrac{32}{\pi}} K_{Ic}$ $[Pa.m^{0.5}]$
- K_I mode I stress intensity factor $[Pa.m^{0.5}]$
- K_{Ic} fracture toughness $[Pa.m^{0.5}]$
- L_* characteristic fracture extension $[m]$
- P_* characteristic fluid pressure $[Pa]$
- Q_{in} fluid rate at the entrance of the fracture $[m^3/s]$
- Q_* characteristic flow rate $[m^3/s]$
- Q_o injection pump rate $[m^3/s]$
- R coordinate of fracture tip $[m]$
- R_f coordinate of fluid front $[m]$
- U injection system compliance $[m^3/Pa]$
- V fluid velocity $[m/s]$
- V_{inj} volume of the injection system $[m^3]$
- W_* characteristic fracture opening $[m]$
- $\mathcal{A}$ dimensionless wellbore radius $[-]$
- $\mathcal{G}_*$ dimensionless groups appearing in the dimensionless system of equations
- $\mathcal{K}$ dimensionless toughness $[-]$
- $\mathcal{L}$ dimensionless initial notch $[-]$
- ℓ_o length of notch transverse to the wellbore $[m]$

- γ dimensionless fracture tip $[-]$

- γ_f dimensionless fluid front $[-]$

- μ_f fluid viscosity $[Pa.s]$

- μ' reduced fluid viscosity $\mu' = 12\mu_f$ $[Pa.s]$

- ν Poisson's ratio $[-]$

- Π_* dimensionless fluid pressure $[-]$

- ρ radial coordinate scaled by the position of the fluid front $[-]$

- σ_o minimum principal stress $[Pa]$

- σ_1, σ_2 maximum and intermediate principal stress $[Pa]$

- χ ratio of time-scales $t_{mk}/t_{\hat{m}\hat{k}}$, evolution parameter governing the transition between compressibility dominated to constant injection regimes $[-]$

- ψ ratio of time-scales t_{mk}/t_{om} evolution parameter related to the disappearance of the fluid lag $[-]$

- Ψ dimensionless fluid rate $[-]$

- Ω_* dimensionless fracture opening $[-]$

- ϑ dimensionless number related to the presence of a fluid lag $[-]$